



BEST1 gene therapy corrects a diffuse retina-wide microdetachment modulated by light exposure

Karina E. Guziewicz^{a,1,2}, Artur V. Cideciyan^{b,1,2}, William A. Beltran^a, András M. Komáromy^{a,c}, Valerie L. Dufour^a, Malgorzata Swider^b, Simone Iwabe^a, Alexander Sumaroka^b, Brian T. Kendrick^a, Gordon Ruthel^d, Vince A. Chiodo^e, Elise Héon^f, William W. Hauswirth^e, Samuel G. Jacobson^b, and Gustavo D. Aguirre^a

^aDivision of Experimental Retinal Therapies, Department of Clinical Sciences and Advanced Medicine, School of Veterinary Medicine, University of Pennsylvania, Philadelphia, PA 19104; ^bScheie Eye Institute, Department of Ophthalmology, Perelman School of Medicine, University of Pennsylvania, Philadelphia, PA 19104; ^cDepartment of Small Animal Clinical Sciences, College of Veterinary Medicine, Michigan State University, East Lansing, MI 48824; ^dDepartment of Pathobiology, School of Veterinary Medicine, University of Pennsylvania, Philadelphia, PA 19104; ^eDepartment of Ophthalmology, College of Medicine, University of Florida, Gainesville, FL 32611; and ^fDepartment of Ophthalmology and Vision Sciences, The Hospital for Sick Children, University of Toronto, Toronto, ON M5G 2L3, Canada

Edited by Jeremy Nathans, Johns Hopkins University, Baltimore, MD, and approved February 8, 2018 (received for review November 27, 2017)

Mutations in the *BEST1* gene cause detachment of the retina and degeneration of photoreceptor (PR) cells due to a primary channelopathy in the neighboring retinal pigment epithelium (RPE) cells. The pathophysiology of the interaction between RPE and PR cells preceding the formation of retinal detachment remains not well-understood. Our studies of molecular pathology in the canine *BEST1* disease model revealed retina-wide abnormalities at the RPE-PR interface associated with defects in the RPE microvillar ensheathment and a cone PR-associated insoluble interphotoreceptor matrix. In vivo imaging demonstrated a retina-wide RPE-PR microdetachment, which contracted with dark adaptation and expanded upon exposure to a moderate intensity of light. Subretinal *BEST1* gene augmentation therapy using adeno-associated virus 2 reversed not only clinically detectable subretinal lesions but also the diffuse microdetachments. Immunohistochemical analyses showed correction of the structural alterations at the RPE-PR interface in areas with *BEST1* transgene expression. Successful treatment effects were demonstrated in three different canine *BEST1* genotypes with vector titers in the 0.1-to-5E11 vector genomes per mL range. Patients with biallelic *BEST1* mutations exhibited large regions of retinal lamination defects, severe PR sensitivity loss, and slowing of the retinoid cycle. Human translation of canine *BEST1* gene therapy success in reversal of macro- and microdetachments through restoration of cytoarchitecture at the RPE-PR interface has promise to result in improved visual function and prevent disease progression in patients affected with bestrophinopathies.

bestrophinopathy | AAV *BEST1* gene therapy | RPE | microvilli | photoreceptors

Inherited retinal degenerations (IRDs) encompass a large group of blinding conditions that are molecularly heterogeneous and pathophysiologically distinct (1, 2). The genetic defect often acts primarily on rod or cone photoreceptors (PRs), or both, and the specific defect may involve phototransduction, ciliary transport, morphogenesis, neurotransmission, or others. Less common are primary defects involving the retinal pigment epithelium (RPE), although they have received increased attention due to high-profile clinical trials (3–5).

The most common IRD due to a primary RPE defect is caused by mutations in *BEST1* (6–8), encoding a transmembrane protein associated with the basolateral portion of the RPE (9–11). *BEST1* acts as a multifunctional channel protein responsible for mediating transepithelial ion transport, regulation of intracellular calcium signaling and RPE cell volume, and modulation of the homeostatic milieu in the subretinal space (10–17). Additional insights supporting *BEST1* function as a calcium-modulated anion channel came from recent crystallographic studies, which revealed a similar structural architecture between avian (18) and bacterial (19) homologs. In eukaryotic cells, *BEST1* forms a stable homopentamer with four transmembrane

helices, cytosolic N and C termini, and a continuous central pore sensitive to calcium-dependent control of chloride permeation (18). Further analysis of *BEST1* structure with targeted mutations has begun to uncover the specific mechanisms responsible for ion selectivity and calcium-mediated activation of this channel protein (20).

In humans, *BEST1* mutations result in a wide spectrum of IRDs collectively grouped as bestrophinopathies that often involve pathognomonic macular lesions (6, 7, 21). Retinal regions away from the lesions tend to appear grossly normal, despite the existence of a retina-wide electrophysiological defect in the electrooculogram, which reflects an abnormality in the standing potential of the eye (21, 22). Naturally occurring biallelic mutations in the canine *BEST1* gene (*cBEST1*) cause canine IRD with distinct phenotypic similarities to both the dominant and recessive forms of human bestrophinopathies, including the

Significance

One of the most common forms of monogenic macular degeneration worldwide is caused by dominant or recessive bestrophinopathies associated with mutations in the *BEST1* gene. Disease expression is known to start with a retina-wide electrophysiological defect leading to localized vitelliform and atrophic lesions and vision loss. To develop lasting therapies for this incurable disease, there is a need for greater understanding of the early pathophysiology before lesion formation. Here we find that the loss of retinal pigment epithelium apical microvilli and resulting microdetachment of the retina represent the earliest features of canine bestrophinopathies. We show that retinal light exposure expands, and dark adaptation contracts, the microdetachments. Subretinal adeno-associated virus-based gene therapy corrects both the vitelliform lesions and the light-modulated microdetachments.

Author contributions: K.E.G., A.V.C., S.G.J., and G.D.A. designed research; K.E.G., A.V.C., W.A.B., A.M.K., V.L.D., S.I., B.T.K., G.R., V.A.C., E.H., W.W.H., S.G.J., and G.D.A. performed research; A.M.K., A.S., and V.A.C. contributed new reagents/analytic tools; K.E.G., A.V.C., W.A.B., V.L.D., M.S., A.S., G.R., and G.D.A. analyzed data; and K.E.G., A.V.C., S.G.J., and G.D.A. wrote the paper.

Conflict of interest statement: W.W.H. and the University of Florida have a financial interest in the use of AAV therapies, and own equity in a company (AGTC, Inc.) that might, in the future, commercialize some aspects of this work.

This article is a PNAS Direct Submission.

This open access article is distributed under Creative Commons Attribution-NonCommercial-NoDerivatives License 4.0 (CC BY-NC-ND).

¹K.E.G. and A.V.C. contributed equally to this work.

²To whom correspondence may be addressed. Email: karinag@vet.upenn.edu or cideciya@pennmedicine.upenn.edu.

This article contains supporting information online at www.pnas.org/lookup/suppl/doi:10.1073/pnas.1720662115/-DCSupplemental.

Published online March 5, 2018.

salient predilection of subretinal lesions to the canine fovea-like area (17, 23, 24).

Proper anatomical apposition and a sustained interaction between RPE apical microvilli (MV) and PR outer segments (OSs) are considered crucial for normal vision. Both the ionic composition and volume regulation of the subretinal space are essential for maintaining the accurate molecular proximity of this complex and homeostasis of the RPE–PR interface (25, 26). In vitro and ex vivo studies have long shown that genetic mutations, metabolic perturbations, as well as light stimuli alter the ionic composition of the subretinal space and physiological responses of the RPE and/or PRs (27–29). More recently, in vivo studies of outer retinal microanatomy in health and disease and its response to light have become increasingly informative with modern retinal imaging modalities (30–40). Here, we combined ex vivo and in vivo approaches to discover and quantify an abnormal modulation of the RPE–PR distance by light exposure in canine bestrophinopathy (cBest). We demonstrate that this is a retina-wide abnormality, and show that adeno-associated virus (AAV)2-mediated *BEST1* gene augmentation corrects this primary subclinical defect as well as the disease.

Results

Early Retina-Wide Pathology at the RPE–PR Interface. To understand the pathophysiology behind the impaired RPE–PR interaction, we first evaluated cBest retinas with clinically obvious disease. The key features of RPE apical membrane responsible for direct interaction with PR OSs were examined by immunohistochemistry (IHC) against EZRIN, a membrane–cytoskeleton linker protein essential for formation of RPE apical MV, and combined with human cone arrestin (hCAR) and peanut agglutinin lectin (PNA) labeling to distinguish the cone PR matrix-specific interface (Fig. 1). Confocal microscopy and analysis of 3D reconstruction images from the wild-type (WT) retina exposed a complex sheet-like structure of both inherent constituents of RPE apical membrane: cone- and rod-associated MV. Cone-MV (also known as RPE apical cone sheath) (41) were more pronounced than rod-MV, and formed a highly organized wrapping that tethered individual cone outer segments (COSs) to the RPE apical surface (Fig. 1*A* and *Movie S1*). In the subretinal space, this intercellular complex was further encased with an equally intricate cone-specific insoluble extracellular matrix sheath (cone-IPM) detected by selective binding of PNA lectin (42) (Fig. 1*A* and *Movie S1*). In diseased cBest retinas, however, such complex extracellular compartmentalization of COSs was lost, and the dearth of microvillar ensheathment was accompanied by hypertrophied RPE cells overloaded with lipofuscin granules and compromised insoluble cone-IPM (Fig. 1*B* and *Movie S2*). These observations were confirmed in three distinct *cBEST1* genotypes (R25*/R25*, P463fs/P463fs, and R25*/P463fs) examined across both the tapetal and nontapetal portions of the retina in 22 eyes after disease onset (age range 45 to 270 wk).

To evaluate the possibility that the structural cone-MV abnormalities are secondary to cone dysfunction and disease, we examined the RPE–COS interaction in a different canine IRD model: a primary cone photoreceptor channelopathy, *CNGB3*-associated achromatopsia (43). We first examined the RPE–COS complex at 6 wk of age; *CNGB3*-mutant retinas, harboring either a missense or locus deletion mutation (43), showed no apparent irregularities at the RPE–PR interface, and the proper localization of RPE apical markers was associated with specific anti-BEST1 labeling (Fig. S1*A* and *B*). Double immunostaining demonstrated specific distribution of EZRIN along cone-MV interdigitating with hCAR-positive yet *CNGB3*-negative COSs (Fig. S1*A* and *B*). Then we studied the consequences of *CNGB3* channel subunit dysfunction in older (ages 57 and 85 wk) mutant retinas, which undergo a gradual cone PR degeneration (44), and found that the microvillar ensheathment of the RPE apical domain still remained largely intact (Fig. S1*C* and *D*).

The findings in *CNGB3*-mutant retinas suggested that the structural alterations associated with cone-MV ensheathment in

cBest were not secondary to a cone defect but specific to the RPE channelopathy triggered by mutations in *BEST1*. We then focused on the 6-wk time point, which is well before clinical disease onset and near the end of postnatal retinal differentiation in dogs (45) (Fig. 1*C* and *D*). In contrast to the age-matched WT control, the lack of specific basolateral BEST1 immunolabeling in the cBest RPE was associated with a rather smooth apical surface and clearly underdeveloped (vestigial) apical microvilli (Fig. 1*C*, arrowheads). Quantification of the spatial density of cone-MV and the length of cone- and rod-MV was performed on deconvolved 3D Z-stack projection images at four retinal locations (Fig. 1*D*). Significant differences ($P < 0.0001$) in the mean number of cone-MV were found between cBest and WT in each retinal region examined (Fig. 1*D*). Even though the cone photoreceptor numbers were comparable to controls, the cone-MV in cBest were much fewer in number, sparsely distributed, and consistently appeared shorter and much finer than those in controls regardless of the topographical location. In control (WT) eyes, the average length of cone-MV was $17.4 (\pm 0.25) \mu\text{m}$ in the tapetal superotemporal quadrant and $12.3 (\pm 0.23) \mu\text{m}$ in the inferior nontapetal retina, whereas the length of rod-MV was $6.7 (\pm 0.11) \mu\text{m}$ and $5.3 (\pm 0.27) \mu\text{m}$ in the tapetal and nontapetal portions of the retina, respectively. In cBest, however, the average length of rare cone-MV extensions identified was substantially reduced (6.0 ± 0.31 and $6.5 \pm 0.74 \mu\text{m}$ in the central tapetal and nontapetal inferior parts, respectively). A quantitative assessment of the minute rod-MV in cBest was beyond the limits of optical resolution.

***cBEST1*-Mutant Eyes Have Retina-Wide Microdetachments That Expand with Light Exposure.** To determine in vivo correlates of the early RPE–PR interface abnormalities detected by IHC, we used non-invasive imaging with optical coherence tomography (OCT) to evaluate cBest eyes at young ages, well before ophthalmoscopic lesions are detectable. Qualitatively, central retinas of all evaluated eyes showed an additional hyposcattering layer in the outer retina located distal to the outer nuclear layer (ONL) that was not detectable in WT eyes (Fig. 2*A*, arrow and double arrow). Unexpectedly, the hyposcattering layer was variable with repeated recordings in the same eye within a single experimental session. Further analyses uncovered that the width of the hyposcattering layer was greater in scans obtained toward the end of an imaging session, when the retina would have been exposed to greater retinal irradiance due to intervening autofluorescence imaging performed with bright short-wavelength lights (Fig. 2*A*, double arrow, more LA). The width of the hyposcattering layer was less in scans obtained early in the imaging session before autofluorescence imaging was performed (Fig. 2*A*, arrow, less LA).

Quantitative studies were performed by obtaining longitudinal reflectivity profiles and making measurements both at nasal and temporal retinal locations. WT eyes ($n = 12$, ages 15 to 17 wk) showed outer retinal hyperscattering peaks at the outer plexiform layer (OPL) and the external limiting membrane (ELM) defining the intervening hyposcattering layer as the ONL (Fig. 2*B*). Distal to the ELM was a hyperscattering peak corresponding to the junction between inner and outer segments of photoreceptors (IS/OS), a major peak originating near the RPE–tapetum interface (RPE/T), and an intervening minor hyperscattering peak corresponding to photoreceptor OS tips, which was often difficult to resolve (Fig. 2*B*). An abnormal hyposcattering layer (Fig. 2*B*, arrows) was detectable in cBest eyes ($n = 6$, age 11 wk) with less light exposure. With greater light exposure, the hyposcattering layer became deeper and more distinct (Fig. 2*B*, double arrows); both nasal and temporal retinal locations showed the same effect. The distance between the IS/OS and RPE/T peaks (Fig. 2*A* and *B*, arrowheads) was measured. In WT eyes, the distance was $41.3 (\pm 4.5) \mu\text{m}$, whereas in cBest eyes this distance was significantly greater ($P < 0.001$) at $46.8 (\pm 6.7) \mu\text{m}$ and $45.2 (\pm 6.8) \mu\text{m}$ (less light exposure) and $55.8 (\pm 10.5) \mu\text{m}$ and $53.5 (\pm 6.3) \mu\text{m}$ (more light exposure) for nasal and temporal retinal regions, respectively (Fig. 2*C*).

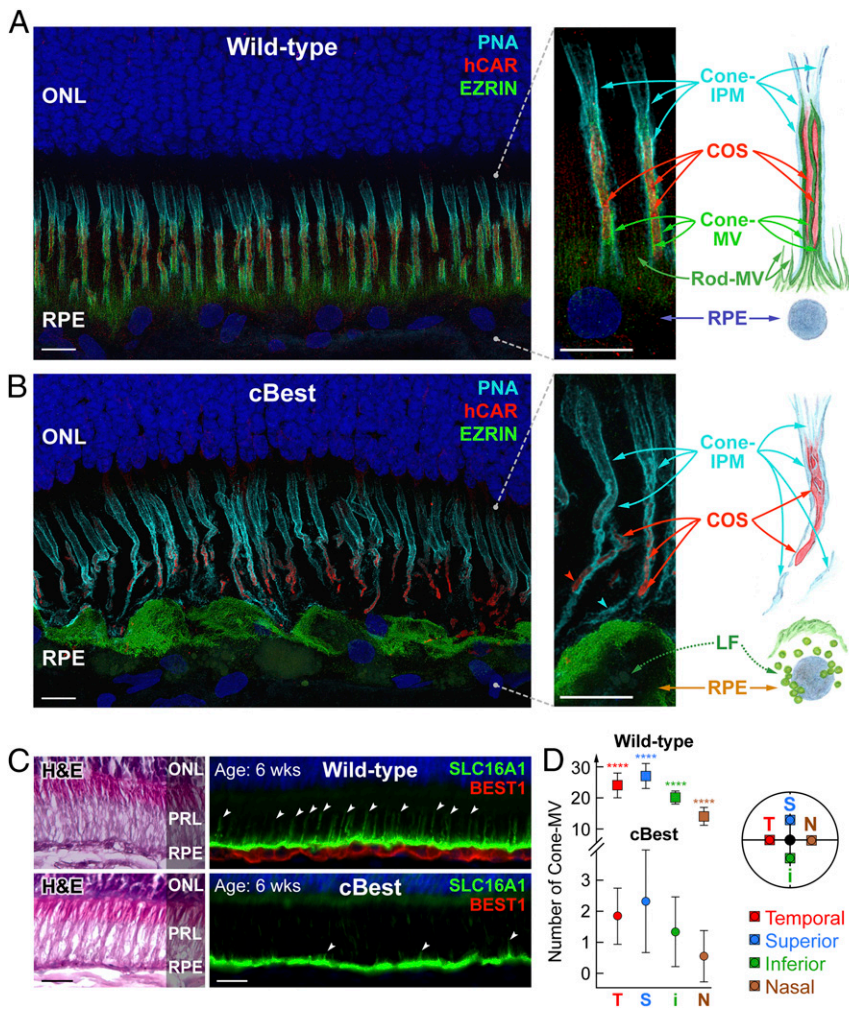


Fig. 1. Retina-wide pathology of RPE apical microvillar projections associated with *BEST1* mutations. (A and B) Confocal images illustrating the molecular pathology of cBest (R25*/R25*; 89 wk) (B) compared with wild-type (A) (42 wk). Retinal cryosections immunolabeled with anti-EZRIN (green) and human cone arrestin (red) and combined with peanut agglutinin lectin (cyan) and DAPI (blue) detail the structural alterations underlying loss of the native extracellular compartmentalization of cone photoreceptor outer segments (B). The RPE apical marker, EZRIN, recognizes both the smaller hair-like projections capping rod OS tips (rod-MV) as well as the more complex and substantial cone-associated MV (cone-MV). The bilayered extracellular ensheathment associated with a single cone OS (COS) is shown in the magnified photomicrographs (Right), along with the corresponding schematic representation. LF, lipofuscin. (Scale bars, 10 μ m.) (C) Representative photomicrographs of 6-wk-old canine wild-type and cBest-mutant (R25*/P463fs) retinas immunolabeled with anti-BEST1 (red) and anti-SLC16A1 (green); white arrowheads point to a subset of cone-MV. H&E, hematoxylin & eosin staining; PRL, photoreceptor IS/OS layer. (Scale bars, 20 μ m.) (D) Quantification of cone-MV numbers across the retina between cBest-mutant and age-matched control eyes. The y axis represents the average number of cone-MV per square millimeter for each color-coded retinal region examined (i, inferior; N, nasal; S, superior; T, temporal) with error bars \pm SD (**** P < 0.0001; n = 80 regions of interest per eye).

Two types of experiments were designed to better understand the thickness of the hyposcattering layer as a function of light exposure. In the main experiment (WT, n = 12, age 15 to 17 wk; cBest, n = 3, age 13 wk), eyes were dark-adapted overnight and then sequential imaging was performed in the dark over a 2-h period with five intervening brief 488-nm light exposures of incrementally greater intensity ranging from very dim lights to moderate lights produced by standard clinical ophthalmic equipment (Fig. 2D). In a shorter experimental protocol, only the highest two light exposures were used in different eyes (cBest, n = 3, age 13 wk). After overnight dark adaptation, IS/OS–RPE/T distance was 40.0 (\pm 4.5) μ m in WT eyes, whereas it was 47.1 (\pm 4.8) μ m in cBest (Fig. 2E); the difference was statistically significant (P < 0.001). Increasingly brighter light exposures resulted in monotonic expansion of the IS/OS–RPE/T distance in cBest eyes, reaching an apparent plateau of 59.4 (\pm 8.7) μ m (Fig. 2E). In WT eyes, the effect of the light exposure was either negligible or small, with the IS/OS–RPE/T distance reaching a plateau of 40.9 (\pm 4.3) μ m. Thus, exposure to light appeared to cause an acute retinal microdetachment of up to 18.4 (\pm 8.7) μ m in cBest eyes within minutes at an age preceding any detectable ophthalmoscopic findings. The light-mediated microdetachment disappeared over a time span of less than 24 h (Fig. S2).

In preparation for localized gene therapy, retinotopic distribution of light-driven microdetachments was evaluated in fully light-adapted cBest and WT eyes (Fig. 2F). The mean IS/OS–RPE/T distance across WT eyes (n = 4, age 104 wk) was relatively homogeneous across superior and inferior retinal areas, with a clear boundary corresponding to the transition between tapetal and

pigmented (nontapetal) retina. Greater distance in the tapetal retina of WT eyes was likely due to differences in the dominant contributors to the hyperscattering peak (tapetum in the tapetal retina versus pigmented RPE). In a cBest eye (R25*/P463fs) at age 297 wk, there was a relatively diffuse retina-wide microdetachment in addition to grossly obvious retinal detachment at the fovea-like region (Fig. 2F, demarcated with purple). In a younger cBest eye (P463fs/P463fs) at age 12 wk, there was a distinct band of greater microdetachment along the visual streak and surrounding the optic nerve head even though no ophthalmoscopic abnormalities were evident. Difference maps between mutant eyes and mean WT demonstrated the spatial distribution of the extent of microdetachments (Fig. 2F, Right).

To assess the potential adverse consequences on photoreceptors, ONL thickness was topographically mapped across the retinal areas with microdetachments (Fig. S3). The microdetachments did not result in thinning of the ONL that would be expected from photoreceptor degeneration. Instead, there was a tendency for the ONL in cBest to be homogeneously thicker than WT; hyperthick regions typically included the central-superior tapetal retina, but could also extend into the inferior nontapetal retina (Fig. S3A). Of importance, the hyperthick regions of the ONL, when examined microscopically, had numbers of PR nuclei that were comparable to controls. This suggests an expansion of internuclear spacing as the likely cause of hyperthick ONL observed by imaging.

Natural History of Canine Bestrophinopathy. As a prerequisite to assessing gene therapy outcomes, the natural history of cBest was determined from a group of 18 dogs [12 male (M) and 6 female

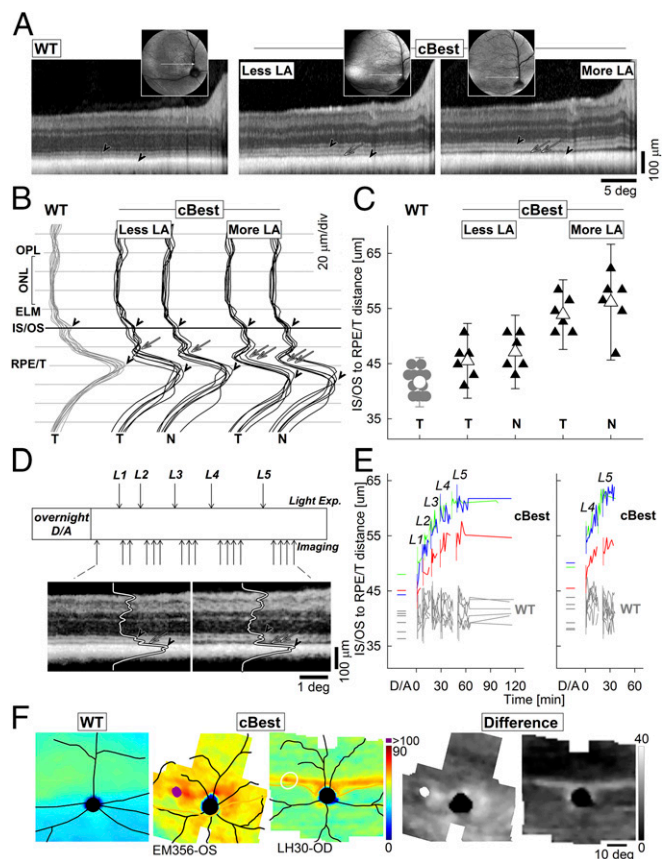


Fig. 2. Light-mediated changes in the outer retinal structure. (A) Cross-sectional imaging along the horizontal meridian through the central area centralis (fovea-like area) in a 15-wk-old normal (WT) dog (Left) and an 11-wk-old cBest (R25*/P463fs) with less (Middle) and more (Right) light adaptation (LA). (Insets) En face reflectance images; the thin white arrows show the superotemporal location of the OCT. The arrowheads and single and double arrows are described in B. (B) Longitudinal reflectivity profiles (LRPs) (average of 85 single LRPs) at 3° nasal from the fovea-like area (T, temporal retina) and nasal edge of the optic nerve head (N, nasal retina) in WT dogs (12 eyes, age 15 to 17 wk) compared with cBest (6 eyes, age 11 wk) with less and more LA. Arrowheads mark IS/OS and RPE/T peaks; single and double arrows mark the additional hyporeflective layer in cBest. (C) Distance between IS/OS and RPE/T peaks in WT and cBest eyes under two LA conditions. Symbols with error bars represent mean (± 2 SD) distance for each group of eyes at both locations. (D, Upper) Schematic description of the dark and light adaptation protocol. Animals were dark-adapted (D/A) overnight and OCT imaging was performed. Then, five increasing light exposures (L1 through L5) were used. Following each light exposure, OCT imaging was repeated. (D, Lower) Magnified views of the OCT scans in cBest with overlapping LRPs after overnight dark adaptation (Left) and after the maximum light exposure (Right). Arrowheads and single and double arrows are described in B. (E, Left) Distance between IS/OS and RPE/T peaks after overnight dark adaptation and following increasing exposures to light (L1 to L5, 488 nm; vertical lines) in cBest ($n = 3$); colored traces represent individual eyes) and WT eyes (gray traces). (E, Right) In a different subset of cBest eyes ($n = 3$; colored traces), results of using an abbreviated protocol involving only L4 and L5 exposures. (F) Spatial topography of IS/OS-to-RPE/T distance in mean WT compared with two representative cBest eyes [pseudocolor panels; EM356-OS: 297-wk-old *cmr1/cmr3* (R25*/P463fs); LH30-OD: 12-wk-old *cmr3* (P463fs/P463fs)]. Purple indicates gross retinal detachment. Grayscale panels show the point-by-point difference between each cBest eye and the mean WT.

(F); age range 6 to 297 wk] (Table S1). cBest dogs were serially monitored by ophthalmoscopy and noninvasive imaging to detect the onset of earliest disease and understand disease progression. Based on the systematic in vivo imaging, the first disease signs were detected as early as 11 wk of age (mean age of 15 wk) as a

subtle focal retinal elevation of the canine fovea-like regions (Fig. S4A). This discrete RPE-PR detachment on cross-sectional imaging, yet unnoticeable on en face imaging, was found to be consistent among cBest eyes examined ($n = 34$), regardless of genotype. From the subclinical stage, the disease progressed to form a macrodetachment (vitelliform stage) limited to the canine fovea and surrounded by microdetachment (Fig. 3A, Left). The primary lesion gradually evolved to manifest as a characteristic bullous detachment within the area centralis that encompassed the fovea-like region (Fig. 3A, Middle and Right and Fig. S4B-D). The presence of distinctive hyperautofluorescence was evident in the inferior part of the lesion (Fig. 3A, Middle Insets; pseudohypopyon stage). The advanced disease stages involved a partial resorption and dispersion of the hyperautofluorescent material within the central lesion, associated with significant thinning of ONL (Fig. S4E and F).

In each case followed by serial imaging (Table S1), cBest manifested bilaterally and nearly always presented a remarkable symmetry, albeit with a variable rate of progression (Fig. 3A and Fig. S4). The gross retinal detachments, ophthalmoscopically visible in both eyes, either remained limited to the central retina or became more extensive with extracentral lesions scattered throughout, still with a strong predilection to the central conerich areas and associated with hyperthick ONL.

Subretinal BEST1 Gene Augmentation Therapy Stably Corrects Disease. To evaluate proof of concept for AAV2-mediated subretinal gene augmentation therapy, 22 cBest eyes were injected [vector titers in the 0.1 to 5E11 vector genomes (vg) per mL range or balanced salt solution (BSS) control] at 27 to 69 wk (Table S1) with a canine (*cBEST1*) or human (*hBEST1*) transgene driven by the human VMD2 promoter (46). cBest dogs exhibiting different stages of focal or multifocal retinal detachments were either injected unilaterally with AAV leaving the fellow eye uninjected, or with AAV in one eye and control (BSS) injection in the contralateral eye; three cases manifesting multifocal disease were injected bilaterally with AAV targeting the superotemporal quadrant, while the retinal areas outside of the surgical bleb served as an internal control (Table S1).

A representative result is shown from a compound heterozygous (R25*/P463fs) dog displaying advanced central retinal detachment in the right eye (EM356-OD) (Fig. 3A) that underwent subretinal injection with *cBEST1* at the age of 52 wk (Fig. 3B, Left), while the fellow eye was not injected (EM356-OS) (Fig. S4). Both eyes were monitored clinically and by in vivo imaging. Disease reversal was first apparent in the injected eye at 4 wk postinjection (p.i.) and retained a sustained effect long-term, as illustrated at 43 and 245 wk p.i. (Fig. 3B). In this and other cases with advanced disease that presented extensive accumulation of autofluorescent material within the subretinal macrodetachments ($n = 13$ eyes), hyperautofluorescent signals were still detectable for several months post AAV injection but gradually faded over time (Fig. 3B, Insets). Based on noninvasive imaging, both the focal as well as extracentral lesions within the AAV-*BEST1*-treated regions resolved 4 to 12 wk p.i., and localized retinal reattachments remained stable thereafter (Table S1). There was no evidence of inflammatory responses in any of the AAV-treated eyes, and the longitudinal in vivo evaluations did not reveal adverse effects on the RPE or neural retina.

AAV-mediated treatment with the *hBEST1* also resulted in lesion reversal and long-term disease correction ($n = 13$ eyes). Representative in vivo imaging results and IHC evaluations (Fig. 3C and D) from a cBest dog (R25*/R25*) showed that the early bilateral lesions present before treatment disappeared after the study eye (EMC3-OS) was treated with AAV-*hBEST1* (2E11 vg/mL) (Fig. 3D), while the lesion in the contralateral control eye (EMC3-OD) injected with BSS continued to enlarge (Fig. 3C). Based on fundusoscopic examination, in the illustrated example as well as in all other cases the transient retinal detachment associated with vector or BSS delivery resolved within 24 to 48 h p.i.; however, the retinal lesions injected with BSS reappeared as early

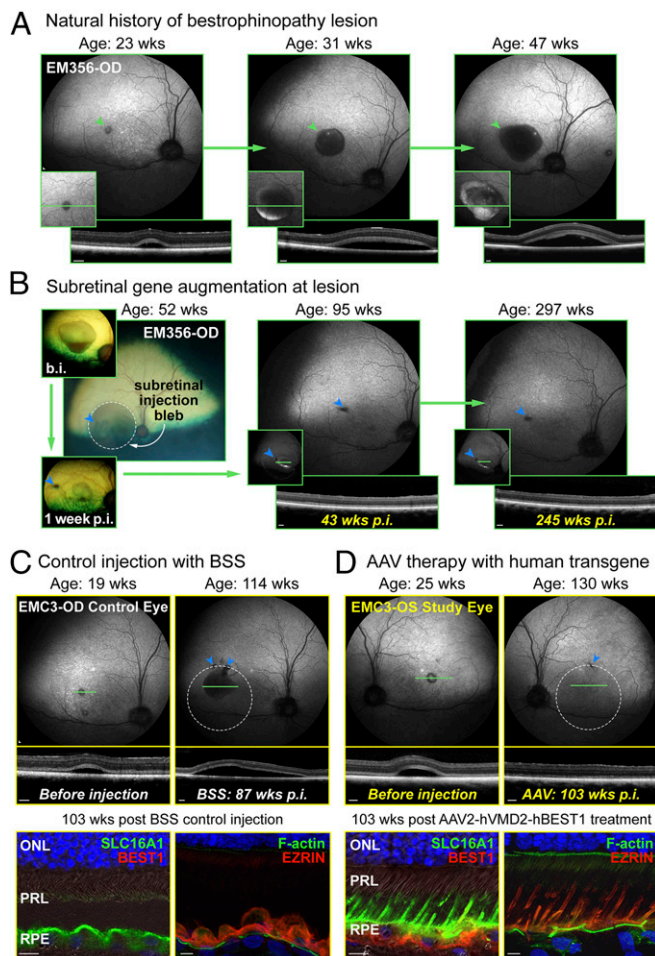


Fig. 3. *BEST1* gene augmentation therapy results in sustained reversal of foveomacular lesions and restoration of RPE-PR interface structure. (A) Natural history of the central subretinal detachment documented by *in vivo* imaging in the right eye of cBest dog (EM356-OD; R25*/P463fs) at three time points. A series of representative near-infrared reflectance (NIR) images demonstrate the evolution of the focal lesion (green arrowhead) in the canine macula from the vitelliform stage (Left) through early pseudohypopyon (Middle) to an advanced pseudohypopyon stage (Right). (A, Insets) Autofluorescence and OCT images. (B) Subretinal injection with AAV2-*cBEST1* (1.5E10 vg/mL) was performed in the eye shown in A at 52 wk of age, entirely encompassing the lesion depicted in the fundus photograph before injection (b.i.) (Left, Upper Inset). The subretinal bleb area is denoted by the dashed circle. The treated eye showed ophthalmoscopic resolution of lesion 1 wk postinjection (p.i.) (Left, Lower Inset); however, confirmatory OCT scans were not available at this age. Images acquired at 43 (Middle) and 245 wk (Right) p.i. document sustained reversal of the central lesion and fully reattached retina within the treated area. (B, Middle and Right, Insets) Autofluorescence and OCT images. EM356-OD and similar labels designate the individual animal and eye. (Scale bars, 200 μ m.) (C and D) Restoration of RPE-photoreceptor interface structure post AAV-*hBEST1* treatment in the cBest (R25*/R25*) model in comparison with control. (C and D, Upper) NIR images from EMC3 eyes exhibiting early vitelliform lesions shown at ages 19 (C) and 25 wk (D). Both eyes were injected at 27 wk of age with either BSS (C; EMC3-OD control eye) or AAV2-*hBEST1* (2E11 vg/mL) (D; EMC3-OS study eye). Bleb boundaries are marked by dashed circles; the locations of corresponding OCT scans cut through the subretinal lesions before injection or through the matching locations mapped p.i. are marked by green horizontal lines; retinotomy sites are indicated by blue arrowheads. (Scale bars, 200 μ m.) (C and D, Lower) Confocal fluorescence images of IHC assessment of AAV-*hBEST1*- or BSS-injected eyes; in contrast to the BSS control eye (C), cytoskeleton rescue and restoration of RPE-PR interface structure are shown in AAV-treated retina 103 wk p.i. (D). (Scale bars, 10 μ m.)

as 1 wk p.i., and progressed along the natural disease course (Fig. 3C). This was in sharp contrast to the AAV-treated eyes, where both the early as well as more advanced lesions resolved within the first 6 wk after *hBEST1* gene therapy, and the treated areas thereafter remained disease-free (Fig. 3D). Ophthalmological examinations and IHC assessments using RPE- and PR-specific markers showed no adverse effects on the retina up to 207 wk p.i. (Fig. 3 and Figs. S5 and S6). Of particular importance, the assessments of the retinal preservation p.i. revealed a remarkable restoration of retinal architecture at the RPE-PR interface, including extension of cone-MV and actin cytoskeleton rescue, corresponding to the vector-treated bleb area with either the canine or human *BEST1* transgenes (Fig. 3C and D, Lower and Figs. S5 and S6). No differences in the clinical picture or response to the AAV-*BEST1* treatment were observed between genders.

Correction of Light-Modulated Microdetachments with Gene Therapy.

To understand the consequences of *BEST1* gene augmentation therapy on retinal regions without ophthalmoscopically detectable retinal detachments, IS/OS-RPE/T distance was measured topographically within and outside subretinal blebs (Fig. 4). A representative result with a control subretinal BSS injection at age 69 wk in a cBest (R25*/P463fs) dog showed homogeneous microdetachment covering all the imaged retina at age 87 wk (Fig. 4A). The average microdetachment extent (IS/OS-RPE/T distance of the BSS-injected mutant dog subtracted from colocalized measurements performed in WT eyes) was 11.6 μ m in the superior retina and 16.7 μ m in the inferior retina (Fig. 4B), consistent with uninjected cBest eyes. Subretinal AAV gene therapy, on the other hand, resulted in substantial reduction of the IS/OS-RPE/T distance in treated regions. EMC3-OS, EML4-OS, and LH21-OS demonstrate results in three genotypes treated with gene therapy using the human *BEST1* transgene with titers of \sim 2E11 vg/mL (Fig. 4A and Table S1). In each case, there was significant reduction of the IS/OS-RPE/T distance in the treated bleb. Notably, gross retinal detachments (purple) were only detectable outside the treatment region (Fig. 4A). Quantitative measurements showed complete amelioration of the microdetachments, with the IS/OS-RPE/T distance returning to WT levels both in superior and inferior retinal regions treated with subretinal gene therapy (Fig. 4B, filled symbols) but not in retinal regions away from the treatment bleb (Fig. 4B, unfilled symbols).

The region of efficacy with subretinal gene therapy is often shown to extend beyond the bleb formed at the time of the surgery to include a penumbral region (47, 48). In cBest dogs with successful gene therapy, there was also a penumbral region but it appeared to be qualitatively larger than typically encountered previously (Fig. 4A). In some of the most extreme examples, pretreatment maps of retina-wide microdetachment were found to be necessary to demonstrate the extent of penumbral expansion. EML9-OD, for example, at age 29 wk showed a retina-wide microdetachment that was most extreme along the visual streak and included several regions with gross retinal detachments (Fig. 4C). Gene therapy was performed at 69 wk. At 87 wk, microdetachments across the whole retina imaged as well as the majority of the gross retinal detachments had disappeared (Fig. 4C), and quantitative measures showed a normal or thinner IS/OS-RPE/T distance in superior and inferior retinal locations (Fig. 4D). Importantly, IS/OS-RPE/T distance showed substantial improvements at retinal locations corresponding to the bleb formed at the time of the injection as well as in nasal retinal control regions in the same eye. This extreme example of penumbral expansion is likely explained by greater diffusion of the vector via the microdetachment in cBest eyes that resulted in the transduction of the RPE at sites substantially more distant than the initial bleb. A more typical example with a delimited penumbral expansion is illustrated for comparison. EML13-OS at age 37 wk showed microdetachments retina-wide that were especially prominent in the temporal retina and along the visual streak; there were also several gross retinal detachments along the visual streak (Fig. 4E). Gene therapy was performed at 45 wk. At 81 wk

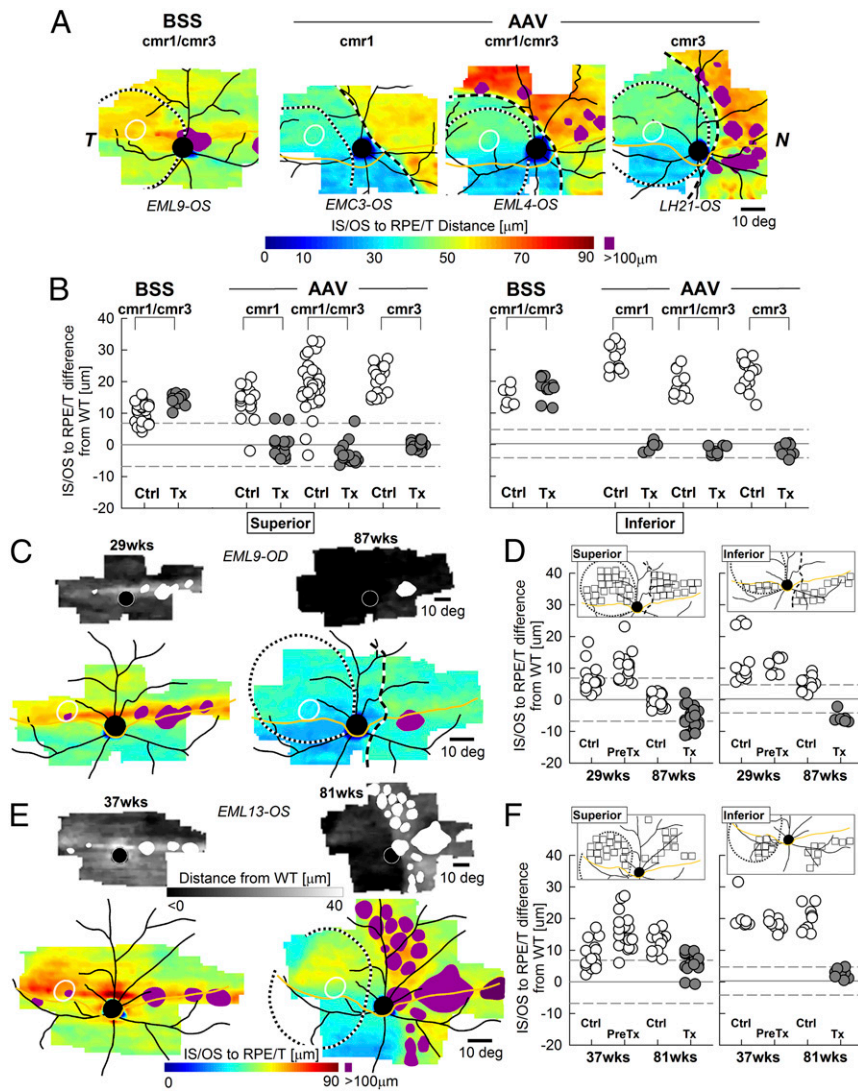


Fig. 4. Reversal of microdetachments across retinal regions after subretinal gene therapy. (A) Pseudocolor maps of IS/OS-RPE/T distance topography in cBest-mutant dogs [*cmr1* (*R25*/R25**), *cmr1/cmr3* (*R25*/P463fs*), or *cmr3* (*P463fs/P463fs*)] subretinally injected with BSS or AAV-h*BEST1*. All imaging was performed in fully light-adapted eyes. Treatment boundaries are based on fundus photographs of the bleb taken at the time of the injection (dotted lines) and, if visible, demarcations apparent at the time of imaging (dashed lines). All eyes are shown as equivalent right eyes with optic nerve and major blood vessels (black), tapetum boundary (yellow), and fovea-like region (white ellipse) overlaid for ease of comparison. EML9-OS and similar labels designate the individual animal and eye. Purple color depicts gross retinal detachment with an IS/OS-RPE/T distance of >100 μ m. (B) The IS/OS-RPE/T distance difference from WT at the superior (Left) and inferior (Right) retinal locations in cBest eyes within the treated bleb (Tx; filled symbols) and untreated outside bleb (Ctrl; open symbols) regions. Dashed lines delimit the 95th percentile of normal variability. All AAV-exposed Tx regions are significantly ($P < 0.001$) different from untreated Ctrl. (C and E) Examples of eyes where the treatment effect extended well beyond the initial treatment bleb. Pseudocolor topographies of the IS/OS-RPE/T distance are shown pre- (Left) and posttreatment (Right). Purple represents gross retinal detachments. (C and E, Upper) Grayscale maps of the difference between each cBest eye and mean WT control. White represents gross retinal detachments. (D and F) Measurements of the colocalized difference of IS/OS-RPE/T distance between WT and cBest pre- (PreTx) and posttreatment (Tx) for the eyes shown in C and E, respectively. (D and F, Insets) Locations sampled within (PreTx and Tx) and outside (Ctrl) the blebs in the superior and inferior retinas. Note that Ctrl regions in EML9-OD show a definite treatment effect likely due to the diffuse microdetachment allowing for widespread vector-driven transduction.

of age, both superior and inferior retina temporal to the optic nerve was lacking micro- and macrodetachments, whereas the untreated nasal retina had retained the microdetachments as well as formed a large number of macrodetachments (Fig. 4E). Quantitative results confirmed the treatment effect (Fig. 4F), which did not reach the nasal retina, unlike EML9-OD.

To understand the potential consequences of gene therapy on retinal degeneration, ONL thickness was mapped across treated eyes (Fig. S3B). Treated retinal regions showing disappearance of microdetachments tended to also correspond to normal ONL thickness, whereas untreated regions retaining microdetachments tended to show hyperthick or normal, or in some regions, thinned ONL (Fig. S3B). In summary, AAV-mediated gene augmentation therapy in canine bestrophinopathies appears to promote a sustained reversal of gross retinal detachments, reestablishment of a close contact between RPE and PRs, and return of ONL thickness to normal values.

Human Autosomal Recessive Bestrophinopathies: Structure and Function. To facilitate clinical translation of successful gene therapy in *BEST1*-mutant dogs, studies were performed to better understand the human pathophysiology of autosomal recessive bestrophinopathies (ARBs) and to gain insight into the distribution of retina-wide disease beyond the gross ophthalmoscopically detectable lesions previously described. Data are shown (Fig. 5) from two patients: P1 was a 39-y-old woman with a best corrected

visual acuity of 20/100 carrying biallelic *BEST1* mutations (c.341T>C/c.400C>G), whereas P2 was a 36-y-old man with 20/60 acuity also carrying biallelic mutations (c.95T>C/c.102C>T) in *BEST1*. In both patients, mutant alleles segregated with clinically unaffected parents. Ultrawide imaging of RPE health taking advantage of the natural autofluorescence of lipofuscin granules they contain showed widespread and extensive abnormalities consisting of regions of relative hyper- or hypoautofluorescence and local heterogeneity. Of note, there was a distinct transition zone (Fig. 5A, arrowheads) in the nasal midperipheral retina demarcating the healthier nasal peripheral retina.

Rod and cone function was sampled at high density along the horizontal meridian to better understand the topography of vision loss and its correspondence to retinal structural abnormalities. Both patients demonstrated a deep (>3 log) loss of rod-mediated sensitivity centrally in long-term dark-adapted eyes; there was relative preservation of rod function in the temporal field (nasal retina) in both patients and the parapapillary area in one patient (Fig. 5B, Upper). Surprisingly, cone-mediated function in light-adapted eyes demonstrated only a moderate loss (<1 log) or normal or near-normal results (Fig. 5B, Lower). Rod and cone function sampled across the full extent of the visual field corroborated and extended these findings and showed strong interocular symmetry (Fig. S7).

Cross-sectional imaging with OCT was performed to evaluate the retinal lamination abnormalities along the horizontal meridian

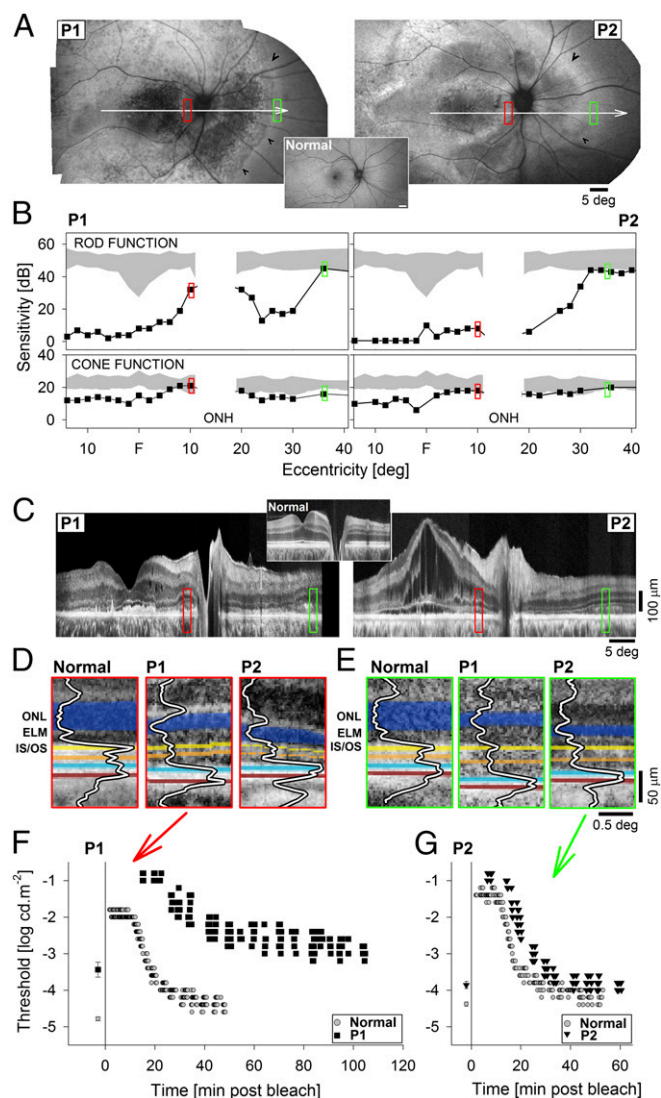


Fig. 5. Retinotypic phenotype in patients with ARB. (A) RPE health across the retinas of two ARB patients, P1 and P2, imaged with short-wavelength reduced-illumination autofluorescence imaging (SW-RAFI), taking advantage of the natural RPE fluorophore lipofuscin. White arrows depict the location of the perimetric profiles and OCT scans; red and green rectangles show the regions of interest shown in other panels; and black arrowheads demarcate disease-to-health transition in the nasal midperipheral retina. (A, *Inset*) Normal SW-RAFI for reference. (B) Perimetric light sensitivity of rods in dark-adapted (*Upper*) and cones in light-adapted (*Lower*) eyes measured across the horizontal meridian. Gray regions represent normal sensitivity except for the physiological blindspot corresponding to the optic nerve (ONH). (C) Retinal cross-section with OCT along the horizontal meridian crossing the fovea. (C, *Inset*) Normal OCT for reference. (D and E) Detail of outer retinal lamination in patients compared with normal at the two regions of interest at the parapapillary retina (D, red) and midperipheral nasal retina (E, green). Layers and peaks are highlighted for visibility. Orange indicates interface near COS tips, blue indicates interface near ROS tips and RPE apical processes, brick indicates interface near the RPE and Bruch's membrane. (F and G) Dark-adaptation kinetics measured in P1 at the parapapillary locus (F) and in P2 at the nasal midperipheral locus (G). Time 0 refers to the end of adaptation light. Baseline thresholds obtained after extended dark adaptation are shown before time 0.

crossing the fovea (Fig. 5C). There was not a consistent light-exposure history at the time of OCT imaging. Both patients showed a significant loss of ONL and abnormalities at the level of photoreceptor IS/OS in the outer retina across most of the central retina. P2, in addition, showed intraretinal cystic spaces

and the detachment of the central retina from the RPE, likely due to accumulation of subretinal fluid. The retinal lamination showed relative normalization in the parapapillary region (Fig. 5C, red rectangles) and beyond the nasal midperipheral transition (Fig. 5C, green rectangles). Analyses of the two regions of interest showed detectable but abnormally thinned ONL, and detectable IS/OS and cone outer segment tip (COST) with low peak signal in both patients (Fig. 5D and E). In P1, the distances from the ELM to IS/OS and IS/OS to COST were comparable to normal. There appeared to be a hyposcattering layer distal to COST, and the RPE appeared hyperthick (Fig. 5D, *Middle*). In P2, ELM to IS/OS appeared shorter than normal, whereas IS/OS-to-COST distance was comparable to normal. COST-to-ROST/RPE distance appeared greater than normal with an intervening indistinct hyposcattering layer; the RPE appeared to be comparable in thickness to normal (Fig. 5D, *Right*). Analysis of the outer retina in the nasal midperipheral region in P1 showed ELM-to-IS/OS, IS/OS-to-COST, and COST-to-ROST/RPE distances greater than normal and RPE thickness which was comparable to normal (Fig. 5E, *Middle*). P2 features appeared intermediate between P1 and normal (Fig. 5E, *Right*).

To understand the implications of structural abnormalities at the level of the outer retina and RPE for the kinetics of retinoid transfer between these cellular layers, dark-adaptation testing was performed. At the parapapillary location shown in Fig. 5D, dark-adapted thresholds of P1 were rod-mediated but 1.3 log unit-elevated (Fig. 5F). By 22.5 min following a light exposure, the P1 results had remained cone-mediated on a plateau whereas normal was already within 1 log unit of the final dark-adapted threshold. By 50 min, P1 rod results were still 1 log-unit elevated whereas normal recovery was complete (Fig. 5F). At the midperipheral nasal retinal location shown in Fig. 5E, dark-adapted thresholds of P2 were rod-mediated and ~ 0.5 log unit-elevated compared with normal (Fig. 5G). By 14.5 min following a light exposure, there was first evidence of rod function which was only incrementally slower than the 11-min cone-rod break in normal. The rate of rod recovery was similar to normal (Fig. 5G). In summary, rod dark-adaptation kinetics of P1 at the parapapillary locus showed an extremely slow time course, whereas dark-adaptation kinetics of rod function of P2 at the midperipheral locus was closer to normal (Fig. 5F and G).

Discussion

The RPE has a key role in maintaining the metabolically active environment of the subretinal space (25, 26, 49). Due to the dynamic relationship with adjacent retinal layers, mutations in RPE-specific genes often adversely affect the neighboring sensory neurons, leading to loss of visual function and PR degeneration (50–52). Mutations in *BEST1* are known to disrupt transepithelial ion and fluid transport in response to abnormal levels of intracellular calcium (11–13). Abnormal RPE calcium signaling is also thought to lead to dysregulation of other pathways through altered expression and interactions of Ca^{2+} -sensitive proteins (20, 53). Based on our findings in cBest, one such protein is EZRIN, a membrane-cytoskeleton linker essential for the formation and proper maturation of RPE apical MV (54–57). It has been demonstrated that the activation of EZRIN's membrane-F-actin cross-linking function occurs directly in response to Ca^{2+} transients (55), and *Ezrin*-KO mice exhibit a substantial decrease in elaboration of RPE MV (57). The apparent underdevelopment of RPE apical MV found in the *BEST1*-mutant RPE is consistent with these reports. Furthermore, our comparative IHC assessments with other IRD models demonstrated that these major structural alterations associated with microvillar ensheathment are specific to the primary RPE channelopathy triggered by *BEST1* mutations, and not secondary to cone dysfunction and degeneration.

The structural components of RPE apical processes are very different from those of nonmotile intestinal microvilli (57–59). The presence of contractile proteins (such as myosin) in the RPE apical microvilli, and also molecules typically found at the sites of

cell attachments, suggests that the RPE actively adheres to, and exerts tension on, the neural retina (58, 59). The dearth of a proper microvillar ensheathment at the RPE–PR interface in cBest, and thus an absence of physical and electrostatic support by these projections to the PR OS, would be expected to weaken the adhesive forces and lead to separation of the RPE–PR complex retina-wide. The microdetachment of the PR layer from the underlying RPE found in cBest at the earliest stages of disease would be consistent with this process. Moreover, the presence of contractile elements in the RPE apical projections and the fact that they have evolved from cells in which pigment migration occurred (58) indicate that MV are capable of active contraction while interdigitating with PR OS, and are destined to facilitate circadian phagocytic activity. A single RPE cell can accommodate about 30 to 50 PRs, depending on the retinal location and packing density (60, 61); the elaborate network of microvilli allows each RPE cell to handle such a high metabolic load on a daily basis. Insights from proteomic profiling support this argument. There is an enriched fraction of retinoid-processing proteins expressed along the RPE apical MV, together with a number of channel proteins and transporters (i.e., Na^+/K^+ ATPase) central to the efficient transport of water, ions, and metabolites between the RPE and PR OS (26, 59). Considering the topographic differences in the size of RPE cells and taking into account the density and length of MV quantified in this study, MV extensions expand the functional surface of a single RPE cell by 20- to 30-fold in the central retina, which is consistent with earlier estimates (62). This number is even higher (~50-fold) for the small RPE cells in the macular region (26, 61, 63) that adapted to a higher turnover rate of shed POS while facing the most densely packed PRs. Such dramatic reduction in a total apical surface area in *BEST1*-mutant RPE will lead to a chronic delay in processing of metabolites, and arrest the abilities of the RPE to maintain both the proper cell volume as well as chemical composition and physiological pH levels in the subretinal space. Since these factors are essential for retinal adhesion (26), any limitation in the RPE transporting system will alter the balance of hydrostatic forces and result in decreased osmoelastic properties of the RPE–PR complex with subsequent separation from the neuroretina. Indeed, the primary serous detachment in human and canine bestrophinopathy is first evident in the fovea, the central area of highest metabolic activity. The absence of high-reaching RPE apical processes, which in the structurally intact retina tightly wrap COS up to the ellipsoids (64), would explain the predilection of this cone-rich structure for its primary detachment in bestrophinopathies. There would be almost exclusive reliance on the frictional interactions with the MV. This is consistent with our observations in cBest, documenting formation of the focal previtelliform lesions within the canine fovea-like area of the area centralis, and also the susceptibility of other central cone-rich areas (like visual streak) to subretinal detachment.

Less expected was the major expansion of microdetachments in cBest upon exposure to dim and moderate light intensities. In normal eyes, light exposure is known to change molecular composition of the subretinal space (65). There is also evidence that measurable structural changes occur in the normal outer retina with light exposure, such as changes in outer segment length (39, 40, 66, 67), hydration of the subretinal space (27–29, 35, 68), increased actin staining along RPE apical MV (37), and phototropism of outer segments (69). However, all of the normal changes are substantially smaller than those measured in cBest. For example, normal human eyes showed changes of ~1 μm (40), and normal mouse eyes showed changes of ~4 μm in the outer retina (37), compared with ~18- μm expansion of the subretinal space driven by light in cBest. Human ARB has only recently been recognized and the literature on the earliest disease stages is limited. Specifically, we are not aware of any ARB literature that has performed quantitative measurements of the outer retina. The recessive cBest disease appears to have phenotypic similarities to both dominant and recessive bestrophinopathies in

humans. In patients with dominant *BEST1* disease (BVMD), there has been some controversy regarding the structural features of retinal regions surrounding vitelliform or later-stage lesions, or retinas in the previtelliform stage of disease. Some studies have demonstrated minor abnormalities at the level of the RPE–PR interface (34, 70, 71), whereas results from others support no detectable structural defects (72–74). Contributing to this controversy could be genotype (75), the resolution of different methodological approaches used, or light history preceding the imaging (36). Indeed, light-dependent outer retinal changes have been described in BVMD using methods like those reported here (36); still, the magnitude of the changes reported in patients was smaller (~2 μm) than in cBest. In general, however, the abnormal response of the affected retina to light stimuli could be related to the markedly reduced light peak/dark trough ratio in the electrooculogram, a finding consistent in all, even presymptomatic, *BEST1* patients.

Of importance, both the micro- and macrodetachments in cBest had adverse effects on photoreceptor health: Regions of microdetachment tended to correspond to hyperthick ONL, whereas large lesions with gross macrodetachment showed thinning of ONL. Smaller lesions with macrodetachment could not be assessed with the sampling methods used here. ONL contains the nuclei of all rods and cones, and classic studies in animal models and human eye donors have generally shown thinning of the ONL with disease progression (76, 77). Less well known are some of the earliest stages of retinal disease showing ONL thickening, which has only become measurable with the advancement of in vivo imaging methods. Human studies have previously demonstrated such ONL thickening in early stages of retinal diseases (78–81). There has also been evidence in animal studies of ONL thickening associated with retinal stress (82). The hyperthick regions of ONL mapped in cBest when examined microscopically showed the number of PR nuclei to be comparable to control, suggesting a greater internuclear spacing within the ONL, likely corresponding to a level of retinal stress that is below the apoptosis threshold. Gross retinal detachments, on the other hand, may cause greater retinal stress and progressive degeneration (17, 83).

To prevent the photoreceptor and vision loss associated with *BEST1* mutations, we performed subretinal gene augmentation therapy directed to retinal areas with macro- and microdetachments. Our results showed that AAV-mediated *BEST1* gene augmentation is safe, reverses the clinically obvious lesions, ameliorates the diffuse microdetachments, and results in normalization of hyperthick ONL. Furthermore, we demonstrated gene therapy success in three distinct *BEST1* genotypes with both focal and multifocal presentations, and confirmed long-term durability of the treatment effect. At the molecular level, we confirmed that both the canine as well as the human *BEST1* transgene can correct the apposition of the RPE–PR complex and restore the cytoarchitecture of this critical interface. Our study suggests that early as well as more advanced stages of autosomal recessive disease are sensible to approach with this therapy. Further studies utilizing human inducible pluripotent stem cell (hiPSC)-derived RPE models derived from patients harboring autosomal dominant *BEST1* mutations (17, 53) will determine whether the gene augmentation approach would also be beneficial for BVMD patients.

To facilitate the clinical translation of successful gene augmentation therapy, ARB patients were studied to gain insight into their retina-wide disease. Consistent with most, but not all, previous descriptions (84–88), retinal disease in our ARB patients extended well beyond the macula into the midperiphery. Our retinotopic mapping of en face and cross-sectional imaging and rod and cone function demonstrated the existence of a distinct transition from disease to health in the midperipheral retina, a feature not previously emphasized. Within the diseased region, severe abnormalities in retinal structure were associated with severe loss of rod function; unexpectedly, cone function was relatively retained. Rod dysfunction within the central retina was also associated with extreme slowing of the retinoid cycle,

whereas the healthier periphery showed near-normal recycling of the retinoids. There are at least two retinoid cycles that provide the 11-*cis*-retinal chromophore to photoreceptor pigments. The canonical retinoid cycle functions in the RPE to produce chromophore for rod and cone PRs (89). The retinal retinoid cycle, on the other hand, is thought to regenerate chromophore within the retina for the specific use of cones (90, 91). The abnormal RPE-PR interface in *BEST1* disease would most likely affect the chromophore delivery from the canonical RPE retinoid cycle; the retinal retinoid cycle may be relatively unaffected, thus explaining the greater retention of cone function.

In summary, our study uncovered new molecular contributors to the pathophysiology of bestrophinopathies at the RPE-PR interface. We discovered the earliest expression of disease: a diffuse microdetachment potentiated by light exposure that was easily detectable by *in vivo* imaging. We showed that AAV-mediated *BEST1* augmentation gene therapy reverses both the grossly obvious lesions and microdetachments, and restores the cytoarchitecture of the RPE-PR interface. Evaluation of ARB patients showed retinotopic distribution and properties of structural and functional defects beyond that expected from PR degeneration. Such visual dysfunction may be expected to improve upon successful application of *BEST1* gene augmentation therapy to patients affected with bestrophinopathies.

Materials and Methods

Human Subjects. Two unrelated patients with ARB were included. Procedures followed the Declaration of Helsinki guidelines. Informed consent was obtained, and all procedures were approved by the Institutional Re-

view Board of the University of Pennsylvania. Patients underwent a complete eye examination and ancillary tests as previously described (92–95). Further experimental details are described in *SI Materials and Methods*.

Canine *BEST1* Models and *In Vivo* Retinal Imaging. cBest-mutant dogs ($n = 18$) of both sexes (12 M and 6 F) harboring either homozygous (c.73C>T) (p.R25*/R25*) or (c.1388delC) (p.P463fs/P463fs) or biallelic (c.73C>T/1388delC) (p.R25*/P463fs) mutations in *cBEST1* (GB*NM_001097545) were included. For ease of annotating the multipanel figures, the three genotypes, respectively, are referred to as *cmr1*, *cmr3*, and *cmr1/cmr3*. The study was conducted in comparison with control cross-bred dogs ($n = 12$; 7 M and 5 F) (Table S1). All animals were bred and maintained at the Retinal Disease Studies Facility (RDSF). The studies were carried out in strict accordance with the recommendations in the *Guide for the Care and Use of Laboratory Animals* of the NIH (96) and in compliance with the Association for Research in Vision and Ophthalmology Statement for the Use of Animals in Ophthalmic and Vision Research. The protocols were approved by the Institutional Animal Care and Use Committee of the University of Pennsylvania (IACUC nos. 804956 and 803422). En face and retinal cross-sectional imaging was performed with the dogs under general anesthesia as previously described (24, 97). Further methodological details are provided in *SI Materials and Methods*.

ACKNOWLEDGMENTS. The authors thank E. V. Dutrow, K. Zorych, E. McTish, and A. Dhingra for excellent technical assistance; Theresa Jordan and RDSF staff for animal care; Drs. J. M. Guzman, F. L. Marinho, and J. C. Chi for assistance in subretinal surgeries; M. Leonard for help in graphic design; and L. Melnyk for research coordination. This work was supported by the Foundation Fighting Blindness: FFB-TRAP and FFB-Facility Grants; Macula Vision Research Foundation; NEI/NIH: EY06855, EY17549, P30-EY001583, R01-EY019304, R01-EY025752-01A1, and S10RR027128; Van Sloun Fund for Canine Genetic Research; and Hope for Vision.

- Bramall AN, Wright AF, Jacobson SG, McInnes RR (2010) The genomic, biochemical, and cellular responses of the retina in inherited photoreceptor degenerations and prospects for the treatment of these disorders. *Annu Rev Neurosci* 33:441–472.
- Veleri S, et al. (2015) Biology and therapy of inherited retinal degenerative disease: Insights from mouse models. *Dis Model Mech* 8:109–129.
- Cideciyan AV (2010) Leber congenital amaurosis due to RPE65 mutations and its treatment with gene therapy. *Prog Retin Eye Res* 29:398–427.
- Ghazi NG, et al. (2016) Treatment of retinitis pigmentosa due to MERTK mutations by ocular subretinal injection of adeno-associated virus gene vector: Results of a phase I trial. *Hum Genet* 135:327–343.
- Russell S, et al. (2017) Efficacy and safety of voretigene neparvovec (AAV2-hRPE65v2) in patients with RPE65-mediated inherited retinal dystrophy: A randomised, controlled, open-label, phase 3 trial. *Lancet* 390:849–860.
- Best F (1905) Über eine hereditäre Maculaaffektion. *Z Augenheilkd* 13:199–212.
- Petrukhin K, et al. (1998) Identification of the gene responsible for Best macular dystrophy. *Nat Genet* 19:241–247.
- Boon CJ, et al. (2009) The spectrum of ocular phenotypes caused by mutations in the *BEST1* gene. *Prog Retin Eye Res* 28:187–205.
- Marmorstein AD, et al. (2000) Bestrophin, the product of the Best vitelliform macular dystrophy gene (VMD2), localizes to the basolateral plasma membrane of the retinal pigment epithelium. *Proc Natl Acad Sci USA* 97:12758–12763.
- Sun H, Tsunenari T, Yau KW, Nathans J (2002) The vitelliform macular dystrophy protein defines a new family of chloride channels. *Proc Natl Acad Sci USA* 99:4008–4013.
- Neusser R, Müller C, Milenkovic VM, Strauss O (2010) The presence of bestrophin-1 modulates the Ca^{2+} recruitment from Ca^{2+} stores in the ER. *Pflugers Arch* 460:163–175.
- Hartzell HC, Qu Z, Yu K, Xiao Q, Chien LT (2008) Molecular physiology of bestrophins: Multifunctional membrane proteins linked to Best disease and other retinopathies. *Physiol Rev* 88:639–672.
- Straub O, Müller C, Reichhart N, Tamm ER, Gomez NM (2014) The role of bestrophin-1 in intracellular Ca^{2+} signaling. *Adv Exp Med Biol* 801:113–119.
- Fischmeister R, Hartzell HC (2005) Volume sensitivity of the bestrophin family of chloride channels. *J Physiol* 562:477–491.
- Milenkovic A, et al. (2015) Bestrophin 1 is indispensable for volume regulation in human retinal pigment epithelium cells. *Proc Natl Acad Sci USA* 112:E2630–E2639.
- Mullins RF, Kuehn MH, Faidley EA, Syed NA, Stone EM (2007) Differential macular and peripheral expression of bestrophin in human eyes and its implication for Best disease. *Invest Ophthalmol Vis Sci* 48:3372–3380.
- Guziewicz KE, et al. (2017) Bestrophinopathy: An RPE-photoreceptor interface disease. *Prog Retin Eye Res* 58:70–88.
- Kane Dickson V, Padi L, Long SB (2014) Structure and insights into the function of a Ca^{2+} -activated Cl^{-} channel. *Nature* 516:213–218.
- Yang T, et al. (2014) Structure and selectivity in bestrophin ion channels. *Science* 346:355–359.
- Vaisey G, Miller AN, Long SB (2016) Distinct regions that control ion selectivity and calcium-dependent activation in the bestrophin ion channel. *Proc Natl Acad Sci USA* 113:E7399–E7408.
- Deutman AF (1969) Electro-oculography in families with vitelliform dystrophy of the fovea. Detection of the carrier state. *Arch Ophthalmol* 81:305–316.
- Arden GB, Constable PA (2006) The electro-oculogram. *Prog Retin Eye Res* 25:207–248.
- Guziewicz KE, et al. (2007) Bestrophin gene mutations cause canine multifocal retinopathy: A novel animal model for best disease. *Invest Ophthalmol Vis Sci* 48:1959–1967.
- Beltran WA, et al. (2014) Canine retina has a primate fovea-like bouquet of cone photoreceptors which is affected by inherited macular degenerations. *PLoS One* 9:e90390.
- Hageman GS, Johnson LV (1991) The photoreceptor-retinal pigment epithelium interface. *Principles and Practice of Clinical Electrophysiology of Vision*, eds Heckenlively JR, Arden GB (Mosby-Year Book, St. Louis), pp 53–68.
- Strauss O (2005) The retinal pigment epithelium in visual function. *Physiol Rev* 85:845–881.
- Huang B, Karwoski CJ (1992) Light-evoked expansion of subretinal space volume in the retina of the frog. *J Neurosci* 12:4243–4252.
- Putting BJ, Zweyffening RC, Vrensen GF, Oosterhuis JA, van Best JA (1992) Blood-retinal barrier dysfunction at the pigment epithelium induced by blue light. *Invest Ophthalmol Vis Sci* 33:3385–3393.
- Li JD, Govardovskii VI, Steinberg RH (1994) Light-dependent hydration of the space surrounding photoreceptors in the cat retina. *Vis Neurosci* 11:743–752.
- Huang Y, et al. (1998) Relation of optical coherence tomography to microanatomy in normal and rd chickens. *Invest Ophthalmol Vis Sci* 39:2405–2416.
- Pianta MJ, et al. (2003) *In vivo* micropathology of Best macular dystrophy with optical coherence tomography. *Exp Eye Res* 76:203–211.
- Cideciyan AV, et al. (2005) *In vivo* dynamics of retinal injury and repair in the rhodopsin mutant dog model of human retinitis pigmentosa. *Proc Natl Acad Sci USA* 102:5233–5238.
- Bizheva K, et al. (2006) Optophysiology: Depth-resolved probing of retinal physiology with functional ultrahigh-resolution optical coherence tomography. *Proc Natl Acad Sci USA* 103:5066–5071.
- Kay CN, et al. (2012) Three-dimensional distribution of the vitelliform lesion, photoreceptors, and retinal pigment epithelium in the macula of patients with best vitelliform macular dystrophy. *Arch Ophthalmol* 130:357–364.
- Bissig D, Berkowitz BA (2012) Light-dependent changes in outer retinal water diffusion in rats *in vivo*. *Mol Vis* 18:2561.
- Abràmoff MD, et al. (2013) Human photoreceptor outer segments shorten during light adaptation. *Invest Ophthalmol Vis Sci* 54:3721–3728.
- Li Y, Fariss RN, Qian JW, Cohen ED, Qian H (2016) Light-induced thickening of photoreceptor outer segment layer detected by ultra-high resolution OCT imaging. *Invest Ophthalmol Vis Sci* 57:OCT105–OCT111.
- Lu Y, Wang B, Pepperberg DR, Yao X (2016) Stimulus-evoked outer segment changes occur before the hyperpolarization of retinal photoreceptors. *Biomed Opt Express* 8:38–47.
- Zhang P, et al. (2017) *In vivo* optophysiology reveals that G-protein activation triggers osmotic swelling and increased light scattering of rod photoreceptors. *Proc Natl Acad Sci USA* 114:E2937–E2946.

40. Lu CD, et al. (2017) Photoreceptor layer thickness changes during dark adaptation observed with ultrahigh-resolution optical coherence tomography. *Invest Ophthalmol Vis Sci* 58:4632–4643.
41. Steinberg RH (1985) Interactions between the retinal pigment epithelium and the neural retina. *Doc Ophthalmol* 60:327–346.
42. Mieziwska K (1996) The interphotoreceptor matrix, a space in sight. *Microsc Res Tech* 35:463–471.
43. Sidjanin DJ, et al. (2002) Canine CNGB3 mutations establish cone degeneration as orthologous to the human achromatopsia locus ACHM3. *Hum Mol Genet* 11:1823–1833.
44. Komáromy AM, et al. (2013) Transient photoreceptor deconstruction by CNTF enhances rAAV-mediated cone functional rescue in late stage CNGB3-achromatopsia. *Mol Ther* 21:1131–1141.
45. Acland GM, Aguirre GD (1987) Retinal degenerations in the dog: IV. Early retinal degeneration (erd) in Norwegian elkhounds. *Exp Eye Res* 44:491–521.
46. Guziewicz KE, et al. (2013) Recombinant AAV-mediated BEST1 transfer to the retinal pigment epithelium: Analysis of serotype-dependent retinal effects. *PLoS One* 8:e75666.
47. Bruewer AR, et al. (2013) Evaluation of lateral spread of transgene expression following subretinal AAV-mediated gene delivery in dogs. *PLoS One* 8:e60218.
48. Beltran WA, et al. (2017) Optimization of retinal gene therapy for X-linked retinitis pigmentosa due to RPGR mutations. *Mol Ther* 25:1866–1880.
49. Sparrow JR, Hicks D, Hamel CP (2010) The retinal pigment epithelium in health and disease. *Curr Mol Med* 10:802–823.
50. Jacobson SG, et al. (2008) Photoreceptor layer topography in children with Leber congenital amaurosis caused by RPE65 mutations. *Invest Ophthalmol Vis Sci* 49:4573–4577.
51. Charbel Issa P, et al. (2009) Characterisation of severe rod-cone dystrophy in a consanguineous family with a splice site mutation in the MERTK gene. *Br J Ophthalmol* 93:920–925.
52. Meunier I, et al. (2016) A dominant mutation in MAPKAPK3, an actor of p38 signaling pathway, causes a new retinal dystrophy involving Bruch's membrane and retinal pigment epithelium. *Hum Mol Genet* 25:916–926.
53. Singh R, et al. (2013) iP5 cell modeling of Best disease: Insights into the pathophysiology of an inherited macular degeneration. *Hum Mol Genet* 22:593–607.
54. Bonilha VL, Finnemann SC, Rodriguez-Boulan E (1999) Ezrin promotes morphogenesis of apical microvilli and basal infoldings in retinal pigment epithelium. *J Cell Biol* 147:1533–1548.
55. Koltzsch M, Neumann C, König S, Gerke V (2003) Ca²⁺-dependent binding and activation of dormant Ezrin by dimeric S100P. *Mol Biol Cell* 14:2372–2384.
56. Bonilha VL, et al. (2006) The retinal pigment epithelium apical microvilli and retinal function. *Adv Exp Med Biol* 572:519–524.
57. Bonilha VL, Rayborn ME, Saotome I, McClatchey AI, Hollyfield JG (2006) Microvilli defects in retinas of ezrin knockout mice. *Exp Eye Res* 82:720–729.
58. Philp NJ, Nachmias VT (1985) Components of the cytoskeleton in the retinal pigmented epithelium of the chick. *J Cell Biol* 101:358–362.
59. Bonilha VL, et al. (2004) Proteomic characterization of isolated retinal pigment epithelium microvilli. *Mol Cell Proteomics* 3:1119–1127.
60. Gao H, Hollyfield JG (1992) Aging of the human retina. Differential loss of neurons and retinal pigment epithelial cells. *Invest Ophthalmol Vis Sci* 33:1–17.
61. Kiser PD, Golczak M, Palczewski K (2014) Chemistry of the retinoid (visual) cycle. *Chem Rev* 114:194–232.
62. Miller SS, Steinberg RH (1977) Passive ionic properties of frog retinal pigment epithelium. *J Membr Biol* 36:337–372.
63. Volland S, Esteve-Rudd J, Hoo J, Yee C, Williams DS (2015) A comparison of some organizational characteristics of the mouse central retina and the human macula. *PLoS One* 10:e0125631.
64. Cuenca N, Ortuño-Lizarán I, Pinilla I (October 13, 2017) Cellular characterization of optical coherence tomography and outer retinal bands using specific immunohistochemistry markers and clinical implications. *Ophthalmology*, 10.1016/j.ophtha.2017.09.016.
65. Uehara F, Matthes MT, Yasumura D, LaVail MM (1990) Light-evoked changes in the interphotoreceptor matrix. *Science* 248:1633–1636.
66. Jonnal RS, Kocaoglu OP, Wang Q, Lee S, Miller DT (2012) Phase-sensitive imaging of the outer retina using optical coherence tomography and adaptive optics. *Biomed Opt Express* 3:104–124.
67. Hillmann D, et al. (2016) In vivo optical imaging of physiological responses to photostimulation in human photoreceptors. *Proc Natl Acad Sci USA* 113:13138–13143.
68. Bialek S, Miller SS (1994) K⁺ and Cl⁻ transport mechanisms in bovine pigment epithelium that could modulate subretinal space volume and composition. *J Physiol* 475:401–417.
69. Lu R, Levy AM, Zhang Q, Pittler SJ, Yao X (2013) Dynamic near-infrared imaging reveals transient phototropic change in retinal rod photoreceptors. *J Biomed Opt* 18:106013.
70. Querques G, et al. (2011) The spectrum of subclinical Best vitelliform macular dystrophy in subjects with mutations in BEST1 gene. *Invest Ophthalmol Vis Sci* 52:4678–4684.
71. Qian CX, et al. (2017) Optical coherence tomography examination of the retinal pigment epithelium in Best vitelliform macular dystrophy. *Ophthalmology* 124:456–463.
72. Kay DB, et al. (2013) Outer retinal structure in best vitelliform macular dystrophy. *JAMA Ophthalmol* 131:1207–1215.
73. Arora R, et al. (2016) Unilateral BEST1-associated retinopathy. *Am J Ophthalmol* 169:24–32.
74. Scoles D, et al. (2017) Photoreceptor inner segment morphology in Best vitelliform macular dystrophy. *Retina* 37:741–748.
75. Abràmoff MD, Mullins RF, Stone EM (2014) Outer segment length in different Best disease genotypes. *JAMA Ophthalmol* 132:1152–1153.
76. Faktorovich EG, Steinberg RH, Yasumura D, Matthes MT, LaVail MM (1990) Photoreceptor degeneration in inherited retinal dystrophy delayed by basic fibroblast growth factor. *Nature* 347:83–86.
77. Milam AH, Li ZY, Fariss RN (1998) Histopathology of the human retina in retinitis pigmentosa. *Prog Retin Eye Res* 17:175–205.
78. Jacobson SG, et al. (2006) Remodeling of the human retina in choroideremia: Rab escort protein 1 (REP-1) mutations. *Invest Ophthalmol Vis Sci* 47:4113–4120.
79. Jacobson SG, Cideciyan AV (2010) Treatment possibilities for retinitis pigmentosa. *N Engl J Med* 363:1669–1671.
80. Cideciyan AV, et al. (2011) Cone photoreceptors are the main targets for gene therapy of NPHP5 (IQCB1) or NPHP6 (CEP290) blindness: Generation of an all-cone Nphp6 hypomorph mouse that mimics the human retinal ciliopathy. *Hum Mol Genet* 20:1411–1423.
81. Sadigh S, et al. (2013) Abnormal thickening as well as thinning of the photoreceptor layer in intermediate age-related macular degeneration. *Invest Ophthalmol Vis Sci* 54:1603–1612.
82. Beltran WA, et al. (2015) Successful arrest of photoreceptor and vision loss expands the therapeutic window of retinal gene therapy to later stages of disease. *Proc Natl Acad Sci USA* 112:E5844–E5853.
83. Johnson AA, et al. (2017) Bestrophin 1 and retinal disease. *Prog Retin Eye Res* 58:45–69.
84. Schatz P, Klar J, Andréasson S, Ponjavic V, Dahl N (2006) Variant phenotype of Best vitelliform macular dystrophy associated with compound heterozygous mutations in VMD2. *Ophthalmic Genet* 27:51–56.
85. Burgess R, et al. (2008) Biallelic mutation of BEST1 causes a distinct retinopathy in humans. *Am J Hum Genet* 82:19–31.
86. Kinnick TR, et al. (2011) Autosomal recessive vitelliform macular dystrophy in a large cohort of vitelliform macular dystrophy patients. *Retina* 31:581–595.
87. Bitner H, et al. (2011) A homozygous frameshift mutation in BEST1 causes the classical form of Best disease in an autosomal recessive mode. *Invest Ophthalmol Vis Sci* 52:5332–5338.
88. Boon CJ, et al. (2013) Autosomal recessive bestrophinopathy: Differential diagnosis and treatment options. *Ophthalmology* 120:809–820.
89. Lamb TD, Pugh EN, Jr (2004) Dark adaptation and the retinoid cycle of vision. *Prog Retin Eye Res* 23:307–380.
90. Wang JS, Kefalov VJ (2011) The cone-specific visual cycle. *Prog Retin Eye Res* 30:115–128.
91. Kaylor JJ, et al. (2013) Identification of DES1 as a vitamin A isomerase in Müller glial cells of the retina. *Nat Chem Biol* 9:30–36.
92. Cideciyan AV, Pugh EN, Jr, Lamb TD, Huang Y, Jacobson SG (1997) Rod plateaux during dark adaptation in Sorsby's fundus dystrophy and vitamin A deficiency. *Invest Ophthalmol Vis Sci* 38:1786–1794.
93. Cideciyan AV, et al. (2000) Rod and cone visual cycle consequences of a null mutation in the 11-cis-retinol dehydrogenase gene in man. *Vis Neurosci* 17:667–678.
94. Cideciyan AV, et al. (2013) Human cone visual pigment deletions spare sufficient photoreceptors to warrant gene therapy. *Hum Gene Ther* 24:993–1006.
95. Cideciyan AV, et al. (2007) Reduced-illumination autofluorescence imaging in ABCA4-associated retinal degenerations. *J Opt Soc Am A Opt Image Sci Vis* 24:1457–1467.
96. National Research Council (2011) *Guide for the Care and Use of Laboratory Animals* (Natl Acad Press, Washington, DC), 8th Ed.
97. Komáromy AM, Varner SE, de Juan E, Acland GM, Aguirre GD (2006) Application of a new subretinal injection device in the dog. *Cell Transplant* 15:511–519.
98. Delori F, et al. (2011) Quantitative measurements of autofluorescence with the scanning laser ophthalmoscope. *Invest Ophthalmol Vis Sci* 52:9379–9390.
99. Beltran WA, Hammond P, Acland GM, Aguirre GD (2006) A frameshift mutation in RPGR exon ORF15 causes photoreceptor degeneration and inner retina remodeling in a model of X-linked retinitis pigmentosa. *Invest Ophthalmol Vis Sci* 47:1669–1681.

Supporting Information

Guziewicz et al. 10.1073/pnas.1720662115

SI Materials and Methods

Human Subjects. Light-adapted and two-color dark-adapted function was measured at 2° intervals across the central visual field (central 60° along horizontal and vertical meridians) and at 12° intervals throughout the visual field. Photoreceptor mediation under dark-adapted conditions was determined by the sensitivity difference between 500- and 650-nm stimuli. Dark-adaptation kinetics was evaluated similar to techniques previously described (92–94) using an LED-based dark adaptometer (Roland Consult) and a short-duration (30 s) moderate light exposure from a clinical short-wavelength autofluorescence imaging device (25% laser output; Spectralis HRA; Heidelberg Engineering). Optical coherence tomography (OCT) was used to analyze laminar architecture across the retina. Retinal cross-sections were recorded with a spectral-domain (SD) OCT system (RTVue-100; Optovue). Postacquisition data analysis was performed with custom programs (MATLAB 7.5; MathWorks). Our recording and analysis techniques have been previously described (30, 31, 94). Longitudinal reflectivity profiles (LRPs) were used to identify retinal features. A confocal scanning laser ophthalmoscope (Spectralis HRA; Heidelberg Engineering) was used to record en face images and estimate RPE health with short-wavelength reduced-illuminance autofluorescence imaging (SW-RAFI) as previously described (95). All images were acquired with the high-speed mode (30° × 30° square field or 50° circular field).

Canine *BEST1* Models and in Vivo Retinal Imaging. Overlapping en face images of reflectivity with near-infrared illumination (820 nm) were obtained (Spectralis HRA + OCT) with 30°- and 55°-diameter lenses to delineate fundus features such as the optic nerve, retinal blood vessels, boundaries of injection blebs, retinotomy sites, and other local changes. Custom programs (MATLAB 7.5; MathWorks) were used to digitally stitch individual photos into a retina-wide panorama. Short-wavelength autofluorescence and reflectance imaging was used to outline the boundary of the tapetum and pigmented RPE. Spectral-domain optical coherence tomography (SD-OCT) was performed with overlapping (30° × 25°) raster scans across large regions of the retina. Postacquisition processing of OCT data was performed with custom programs (MATLAB 7.5). For retina-wide topographic analysis, integrated backscatter intensity of each raster scan was used to position its precise location and orientation relative to the retinal features visible on the retina-wide mosaic formed by near-infrared reflectance (NIR) images. Individual LRPs forming all registered raster scans were allotted to regularly spaced bins (1° × 1°) in a rectangular coordinate system centered at the optic nerve; LRPs in each bin were aligned and averaged. Intraretinal peaks and boundaries corresponding to the OPL, ELM, IS/OS, and RPE/T were segmented using both intensity and slope information of backscatter signal along each LRP. Topographic maps of ONL thickness were generated from the OPL-to-ELM distance, and maps of IS/OS-to-RPE/T thickness were generated from the distance between these peaks. For all topographic results, locations of blood vessels, optic nerve head, bleb, tapetum boundaries, and fovea-like area (24) were overlaid for reference. First, maps from WT dogs were registered by the centers of the optic nerve head and rotated to bring the fovea-like areas in congruence, and a map of mean WT topography was derived. The fovea-like area of cBest-mutant dogs was determined by superimposing a WT template onto mutant eyes by alignment of the optic nerve head, major superior blood vessels, and boundary of the tapetum. Next,

cBEST1-mutant maps were registered to the WT map by the center of the optic nerve and estimated fovea-like area, and difference maps were derived. Difference maps were sampled within and outside treatment blebs for each eye. The relation between exposure to light and changes to outer retinal structure was evaluated by two approaches. In a subset of eyes, cross-sectional OCT imaging was performed early in each experimental session followed initially by autofluorescence imaging with a bright short-wavelength light followed subsequently by further OCT imaging. OCT records obtained early in such sessions were considered to be from retinas exposed to less light compared with records obtained late, although the exact light exposure could not be quantified. In another subset of eight eyes, OCT recordings were performed after overnight dark adaptation, and serially in a dark room following short intervals of short-wavelength light exposure from a cSLO. In three of the eyes, five increasingly greater light exposures were used: L1: laser, 20%; duration, 60 s; L2: laser, 25%; duration, 30 s; L3: laser, 50%; duration, 30 s; L4: laser, 100%; duration, 30 s; L5: laser, 100%; duration, 300 s. In three eyes, only L4 and L5 were used. In two additional eyes, only L5 was used to follow the recovery of light-mediated microdetachment over a 24-h period. The standard (100%) laser setting is estimated to correspond to a human retinal irradiance of 330 $\mu\text{W}\cdot\text{cm}^{-2}$ at 488-nm wavelength (98). In both approaches, the areas selected for analysis were based on near-infrared imaging of the fundus with the cSLO before the start of the study, and excluded areas where overt clinically visible macrodetachments were located.

Subretinal Injections and Postoperative Procedures. Subretinal injections of recombinant AAV2/2 delivering either the *cBEST1* or *hBEST1* transgene under control of the human VMD2 promoter (46) were performed under general anesthesia following previously published procedures (46, 82, 97). Vector production and validation have been detailed previously (46). Injection volumes ranging from 50 to 180 μL of the viral vector solution (titer range of 0.1 to 5E11 vg/mL) (Table S1) were delivered subretinally using a custom-modified RetinaJect subretinal injector (SurModics) (97) under direct visualization with an operating microscope via a transvitreal approach without vitrectomy. An anterior chamber paracentesis was performed immediately after injection to prevent increase in intraocular pressure. Directly after injection, formation of a subretinal bleb was documented by fundus photography (RetCam Shuttle; Clarity Medical Systems). In all cases, the surgical bleb flattened and the retina reattached within 24 to 48 h p.i. Ophthalmic examinations, including biomicroscopy, indirect ophthalmoscopy, and fundus photography, were conducted on a regular basis (24 h, 48 h, and 5 d p.i., and then weekly for the first 2 mo followed by a monthly eye examination thereafter) throughout the injection–end point evaluation time interval. Postoperative management was performed as described previously (46).

Histological and Immunohistochemical Evaluations. Ocular tissues for ex vivo analyses were collected as previously described (24, 99). All efforts were made to improve animal welfare and minimize discomfort. For all ex vivo assessments, cBest and control (WT) eyes were fixed in 4% paraformaldehyde, embedded in optimal cutting temperature media, and processed as reported previously (99). Histological assessments were made using standard hematoxylin/eosin (H&E) staining, and all immunohistochemical experiments were performed on 10- μm -thick cryosections following established protocols (46, 99). Briefly, retinal

cryosections were permeabilized with 1× PBS/0.25% Triton X-100, blocked for 1 h at room temperature, and incubated overnight with a primary antibody (Table S2). For multicolor labeling, primary antibodies were combined with Alexa Fluor 488 phalloidin (Thermo Fisher Scientific) or PNA-AF647 (L32460; Molecular Probes), followed by incubation with a corresponding secondary antibody (Alexa Fluor) for 1 h. The slides were examined by epifluorescence or transmitted light microscopy (Axioplan; Carl Zeiss Meditec), and digital images were collected with a Spot 4.0 camera (Diagnostic Instruments).

Confocal Microscopy and Image Analysis. Confocal images were acquired on a TCS-SP5 confocal microscope system (Leica Microsystems) or an A1R laser scanning confocal microscope

(Nikon Instruments). To obtain counts of cone-associated MV (cone-MV), two adjacent fields, each region of interest (ROI) 155 μm long, were imaged 4 mm from the optic nerve head in 10 retinal sections per retinal quadrant (temporal, superior, inferior, and nasal) ($n = 80$ ROIs per eye) in both eyes from 6-wk-old cBest (R25*/P463fs) and an age-matched WT control. Image stacks were acquired at 0.25- μm Z-steps and deconvolved with Huygens deconvolution software version 17.04 (Scientific Volume Imaging). All deconvolved images were rendered in the Leica LAS X 3D rendering module, where the cone-MV were counted manually. The length of both cone- and rod-MV was assessed within the Leica LAS X software from maximum-projection images. Data were analyzed in Microsoft Excel and quantified using Prism software version 7 (GraphPad).

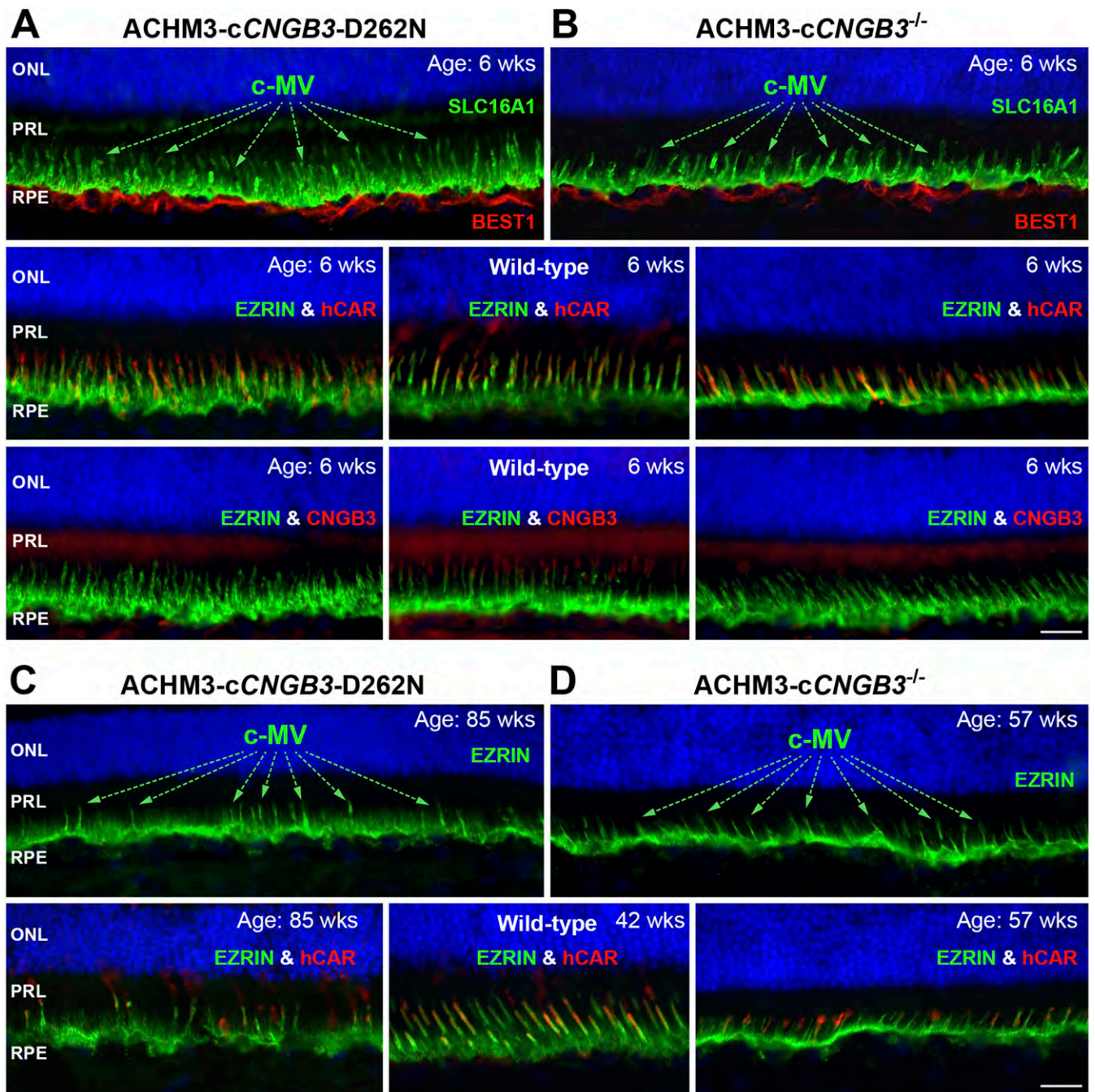


Fig. S1. RPE-PR interdigitation zone in canine models of *CNGB3*-associated achromatopsia (ACHM3). (*A* and *B*, *Upper*) Representative fluorescence microscopy images of 6-wk-old *CNGB3*-D262N-mutant (*A*) and *CNGB3*-null (*B*; *CNGB3*^{-/-}) retinas demonstrating normal expression of BEST1 (red) limited to the basolateral plasma membrane of RPE cells, and SLC16A1 (green), a marker labeling RPE apical processes. Arrows point to a subset of cone-associated RPE apical microvilli (c-MV). (*Middle*) RPE apical surface in *CNGB3*-mutant retinas immunolabeled with EZRIN (green) and hCAR (red). (*Lower*) Anti-*CNGB3* (red) and anti-EZRIN (green) colabeling. An age-matched wild-type retina is shown for reference. Note the lack of *CNGB3*-positive COS in the presence of a structurally intact RPE apical surface. (Scale bar, 20 μ m.) (*C* and *D*) Immunohistochemical evaluation of the RPE-PR interface in *CNGB3*-mutant retinas from 85-wk-old (*C*) and 57-wk-old (*D*) affected dogs. (*C* and *D*, *Upper*) RPE apical aspect and its microvillar extensions are immunolabeled with EZRIN (green), and a subset of c-MV is denoted by green arrows. (*C* and *D*, *Lower*) Double immunostaining of hCAR (red) and EZRIN (green) in retinal cryosections from adult *CNGB3*-mutant dogs. Note the c-MV (green) projecting into the subretinal space despite the gradual deterioration and loss of COS (red). hCAR-EZRIN colabeling in the wild-type retina is shown for comparison. (Scale bar, 20 μ m.) ACHM3, achromatopsia type 3 (MIM*262300); c*CNGB3*, canine *CNGB3* gene; c-MV, cone-associated RPE apical microvilli; *CNGB3*, cyclic nucleotide-gated channel beta 3 protein; hCAR, human cone arrestin; ONL, outer nuclear layer; PRL, photoreceptor inner and outer segment layer; RPE, retinal pigment epithelium; SLC16A1, solute carrier family 16 member 1.

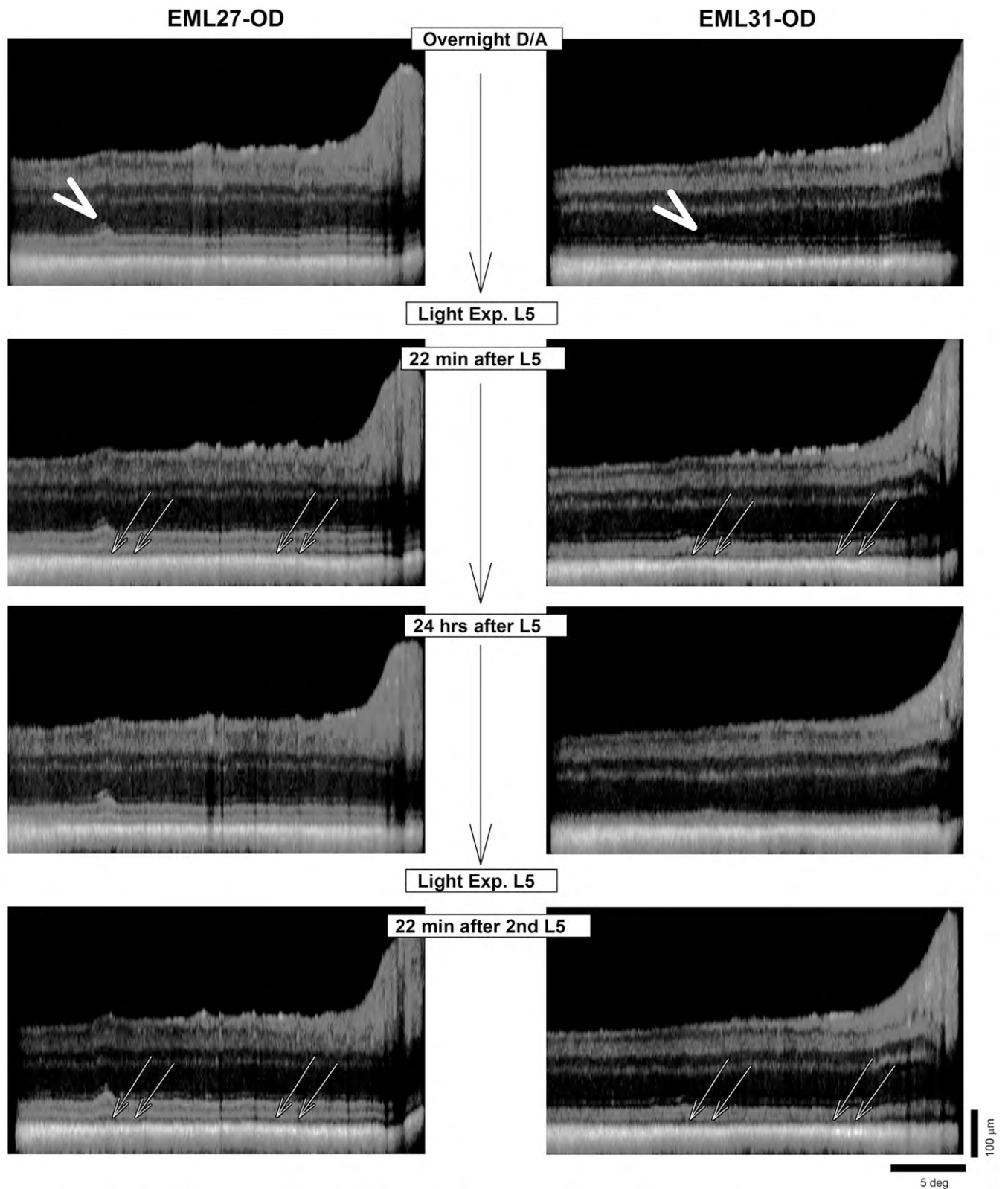


Fig. S2. Recovery of light-mediated microdetachments. Two cBest-affected ($R25^*/P463fs$) eyes [ages 43 (*Right*) and 52 (*Left*) wk] were dark-adapted overnight and imaged similar to results shown in Fig. 2. The eyes were exposed to L5 level and imaged in the dark at 22 min after the onset of the light (second row), and 24 h later after overnight dark adaptation (third row). L5 exposure was repeated on the second day (fourth row). The first exposure resulted in a $6.8 (\pm 4.1)\text{-}\mu\text{m}$ expansion (double arrows) of the IS/OS-to-RPE/T distance at 22 min after the onset of L5. After 24 h of dark adaptation, IS/OS-to-RPE/T distance had returned to baseline conditions. A second L5 exposure resulted in a similar response, demonstrating the repeatability of light-mediated microdetachments. White arrowheads indicate fovea-like areas. Optic nerve head is visible at the right edge of each scan.

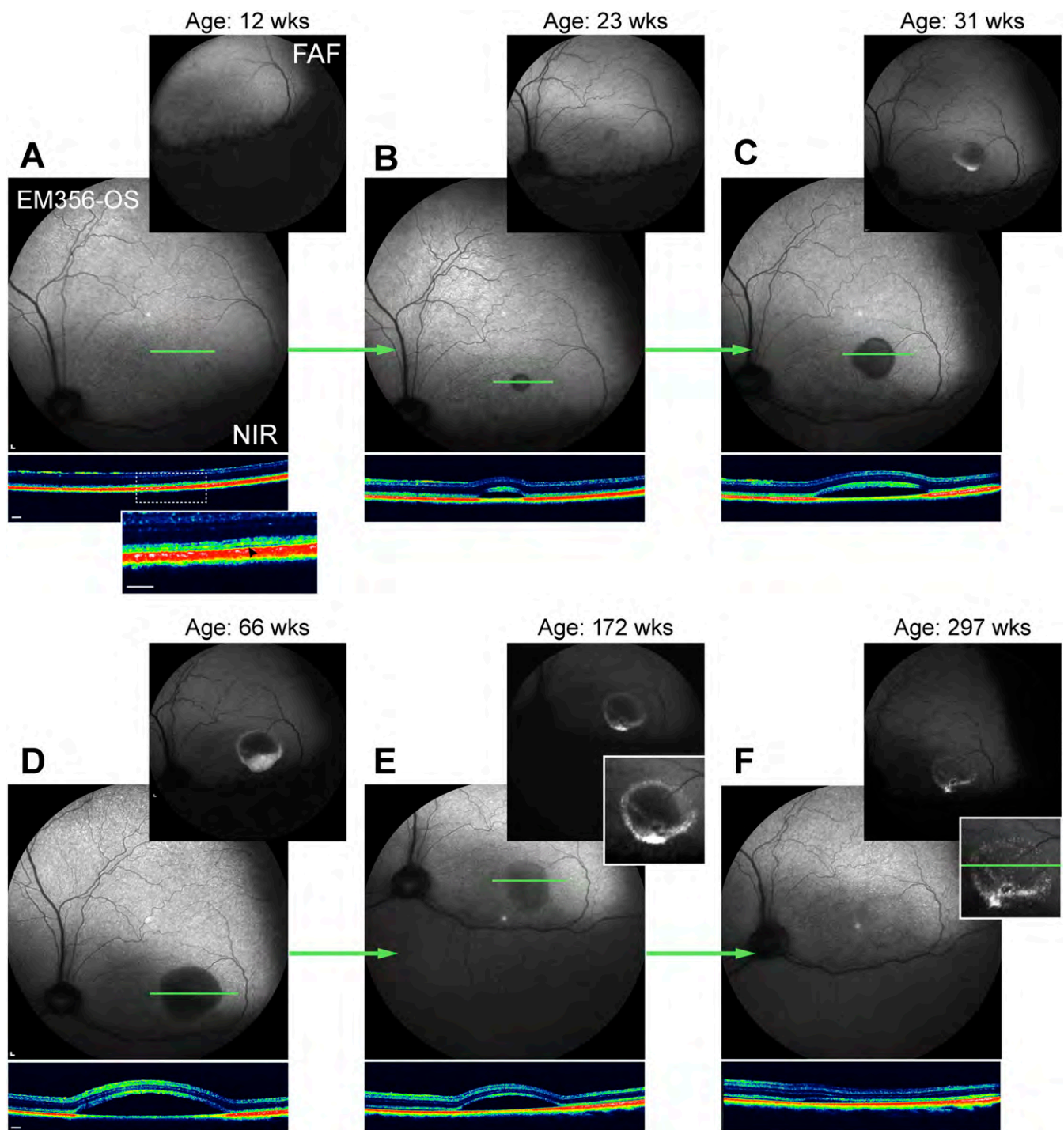


Fig. S4. Evolution of a focal macular lesion in cBest. Representative en face and cross-sectional images of a left eye from a cBest-affected (R25*/P463fs) dog (EM356-OS). A subtle elevation of retinal surface focal to the canine fovea is shown in the magnified SD-OCT image (*Inset*, black arrowhead), although not appreciable en face [NIR or fundus autofluorescence (FAF)] (A). This discrete separation of photoreceptor layer from the underlying RPE progressed to form a larger subretinal macrodetachment (vitelliform lesion) evident en face and on the corresponding OCT scan at 23 wk of age (B). The first signs of hyperautofluorescent material accumulating within the subretinal lesion were observed 8 wk later (C; 31 wk; early pseudohypopyon lesion). At 66 wk of age, a typical pseudohypopyon appearance is documented (D), followed by vitelliruptive-like lesions at 172 and 297 wk of age with dispersion of the autofluorescent material (*Insets*, close-ups) and significant thinning of the ONL apparent by OCT scan (E and F). Green lines demarcate the position of the corresponding SD-OCT scans. cSLO/SD-OCT. (Scale bars, 200 μ m.)

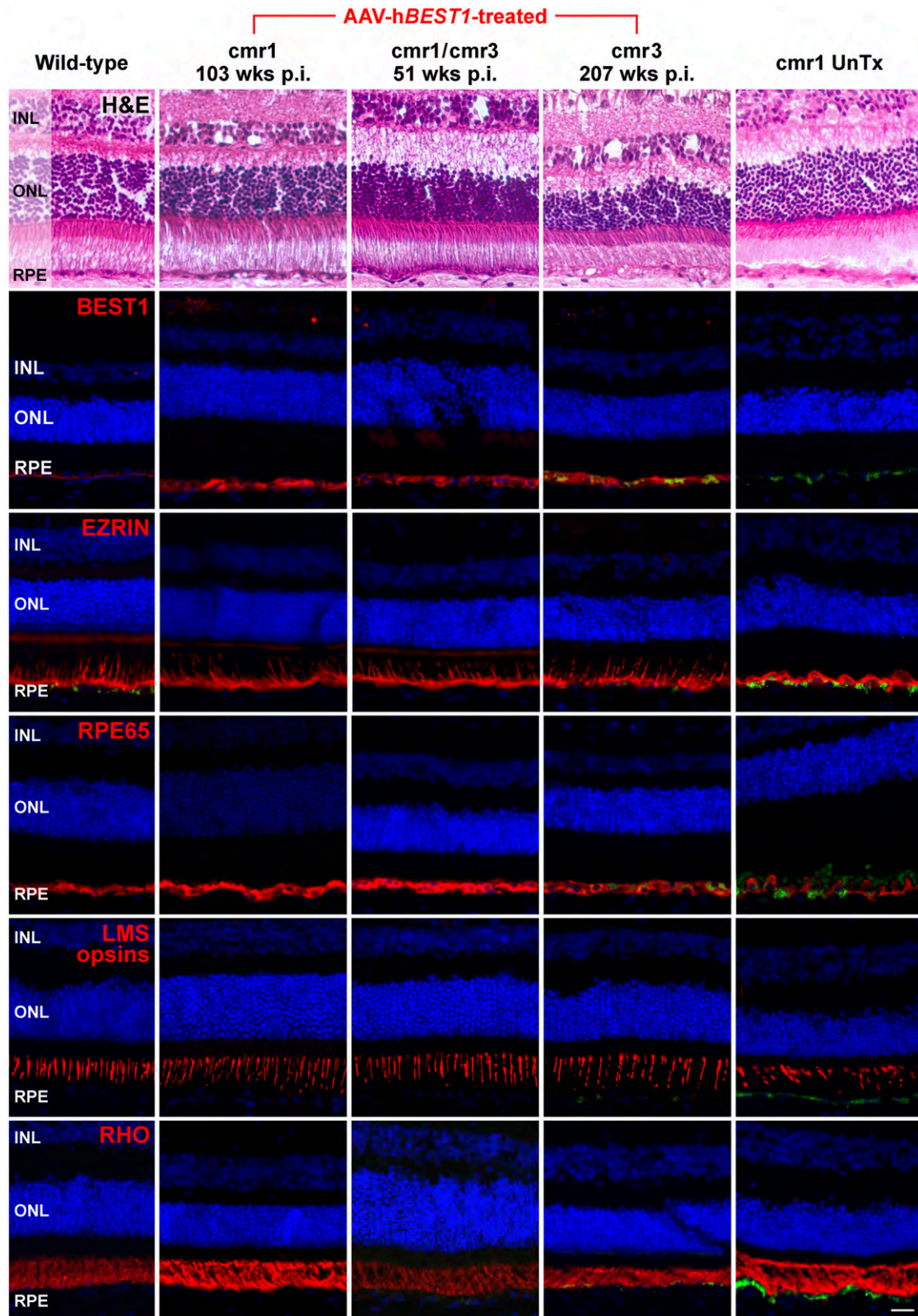


Fig. 55. Retinal preservation after AAV-hBEST1 treatment. A representative IHC summary of retinal preservation assessed post AAV-hBEST1 therapy in three cBest models [*cmr1* (R25*/R25*), *cmr1/cmr3* (R25*/P463fs), and *cmr3* (P463fs/P463fs)] in comparison with the wild-type control (*Far Left*) and cBest untreated (*cmr1* UnTx) (*Far Right*) eyes. cBest eyes were injected with AAV-hBEST1 (2E11 vg/mL) at 27 wk (*cmr1*), 45 wk (*cmr1/cmr3*), or 63 wk (*cmr3*) of age, and evaluated by IHC at 103 wk, 51 wk, or 207 wk p.i., respectively. No apparent abnormalities within the treated areas were detected up to 207 wk p.i. Note the RPE apical extensions projecting into subretinal space in all treated eyes (EZRIN). The untreated cBest control (*Far Right*) shows lack of RPE apical microvilli, RPE hypertrophy (EZRIN, RPE65), and accumulation of lipofuscin granules within the RPE monolayer along with autofluorescent deposits in the subretinal space (endogenous; green). hBEST1, human BEST1 transgene; INL, inner nuclear layer. (Scale bar, 20 μ m.)

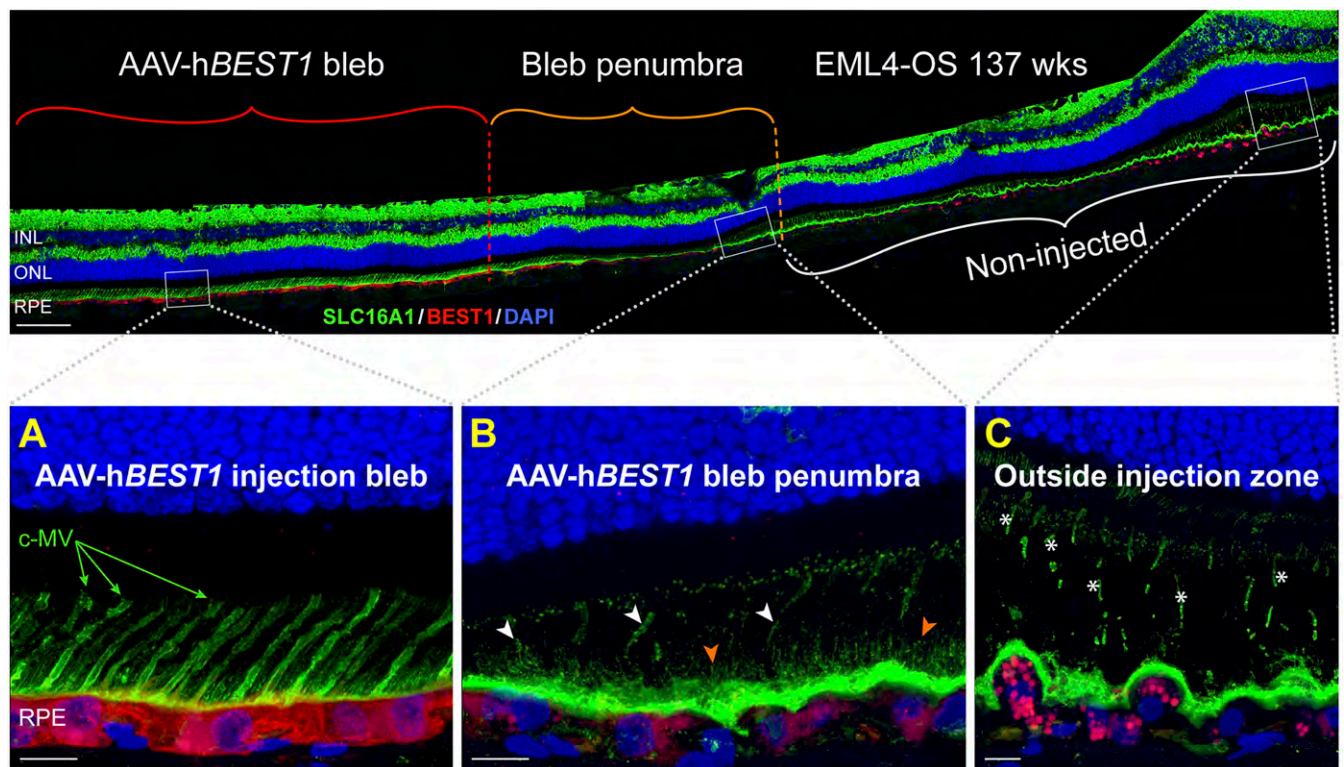


Fig. S6. Dose–response effects of *BEST1* transgene expression on RPE cytoskeleton rescue. Representative confocal photomicrographs depicting a cBest (R25*/P463fs) retina 79 wk post AAV-h*BEST1* injection (2.5E11 vg/mL) and double-labeled with *BEST1* (red) and *SLC16A1* (green). (*Upper*) Cross-sectional overview from the surgical bleb area (*Left*), through the adjacent penumbral region (*Middle*), and toward the contiguous extent outside of the injection zone (*Right*). A direct correlation between the degree of restoration of the RPE–PR interface structure and *BEST1* transgene expression was observed as highlighted in the magnified images. Note the remarkable extension of RPE apical projections within the treated region with augmented *BEST1* (*A*); presence of vestigial microvilli [c-MV (white arrowheads) and rod-MV (orange arrowheads)] in the bleb penumbra associated with patchy distribution of *BEST1* (weak red signals within individual RPE cells) and RPE–PR microdetachment (*B*); formation of subretinal lesions in the absence of both *BEST1* expression and RPE apical processes outside of the treatment zone (*C*). Note the scalloped and unelaborated RPE apical surface (*C*) and massive intracellular deposits that appear as granular aggregates (magenta) within cBest mutant RPE (noninjected *Upper*; *C*, close-up). In the zone of detachment, cellular debris creeping into subretinal space (asterisks) corresponds to the Muller glia, and reflect retinal remodeling in response to stress. [Scale bars, 100 μ m (*Upper*) and 10 μ m (*A–C*).]

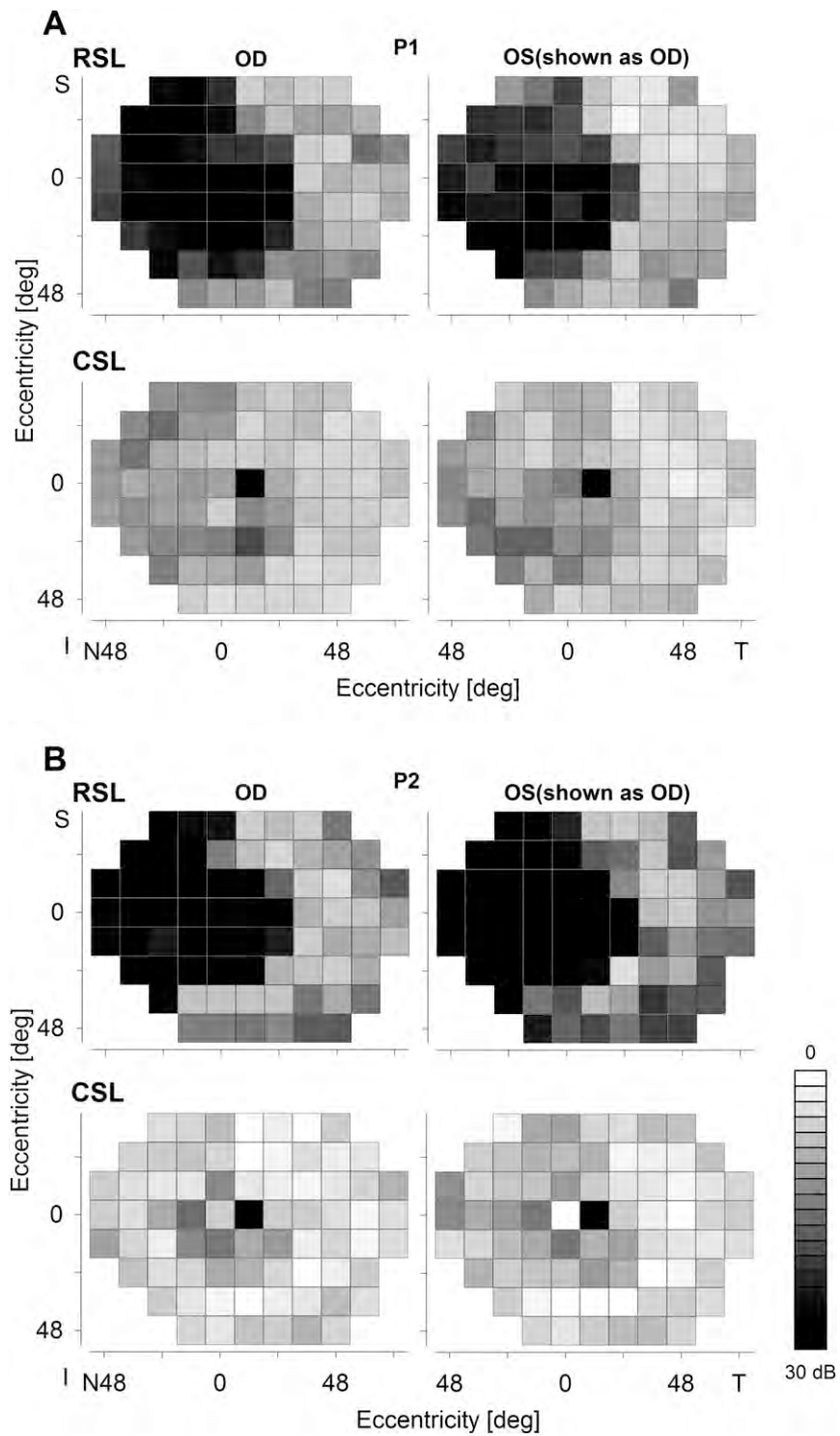


Fig. S7. Interocular symmetry of rod and cone function ARB patients P1 (A) and P2 (B). Rod (RSL) and cone sensitivity loss (CSL) maps of both eyes of two patients with ARB. There are large and symmetric central areas of severe RSL surrounded by relatively retained function in the temporal field (*Upper maps*). Cone function is relatively less affected and CSL is relatively uniform across the visual fields (*Lower maps*). Physiological blind spot is shown as black square at 12° in the temporal field. OD, right eye; OS, left eye.

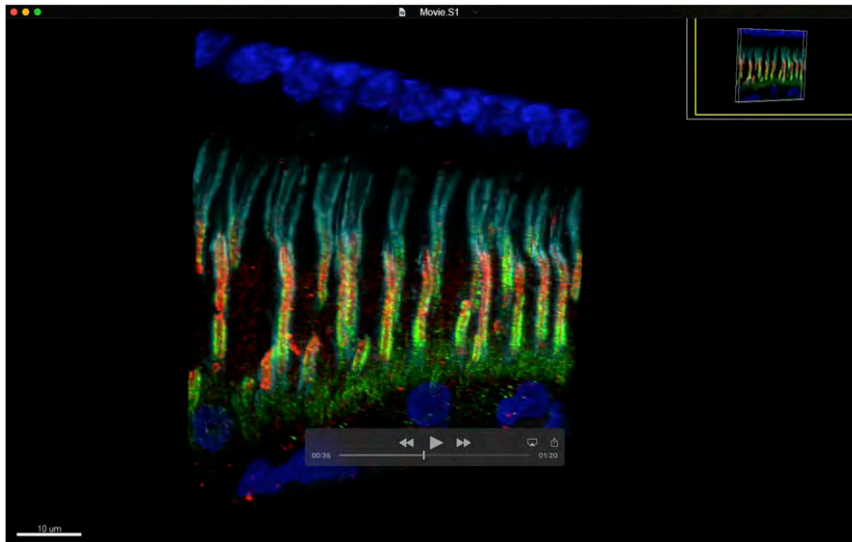
Table S1. Summary of AAV-BEST1-treated and control eyes used in the study

Dog ID	Sex	cBEST1 status	Eye	Treatment	Age, wk	AAV titer inj., vg/mL	Volume inj., μ L	Last examination, wk p.i.	Outcome
EM356	M	R25*/P463fs	OD	AAV-cBEST1	52	1.5E+10	50	245	Reversal
			OS	UnTx				245	Progression
EM385	M	R25*/R25*	OD	BSS	39		50	105	Progression
			OS	AAV-cBEST1	39	1.5E+11	60	105	Reversal
EMC1	F	R25*/R25*	OD	AAV-hBEST1	27	2.0E+11	110	156	Reversal
			OS	BSS				27	110
EMC3	F	R25*/R25*	OD	BSS	27		110	103	Progression
			OS	AAV-hBEST1				27	2.0E+11
EML4	M	R25*/P463fs	OD	BSS	58		150	79	Progression
			OS	AAV-hBEST1				58	2.5E+11
EML6	F	R25*/P463fs	OD	AAV-hBEST1	43	2.0E+11	100	51	Reversal
			OS	BSS				43	110
EML9	M	R25*/P463fs	OD	AAV-hBEST1	69	5.0E+11	65	54	Reversal
			OS	BSS				69	70
EML13	F	R25*/P463fs	OD	UnTx				52	Progression
			OS	AAV-hBEST1				45	1.5E+11
EML22	F	R25*/P463fs	OD	AAV-hBEST1	27	3.5E+11	100	39	Reversal
			OS	AAV-hBEST1				27	3.5E+11
LH15	M	P463fs/P463fs	OD	AAV-hBEST1	65	2.5E+11	180	207	Reversal
			OS	AAV-hBEST1				65	2.5E+11
LH21	M	P463fs/P463fs	OD	BSS	27		50	207	Progression
			OS	AAV-hBEST1				27	2.5E+11
LH30	M	P463fs/P463fs	OD	AAV-hBEST1	31	2.5E+11	110	13	Reversal
			OS	AAV-hBEST1				31	2.5E+11
AS277	M	WT	OU	UnTx control	6				
EML24	M	R25*/P463fs	OU	UnTx control	6				
EML21	M	R25*/P463fs	OU	UnTx control	13				
EML23	F	R25*/P463fs	OU	UnTx control	13				
N306	M	WT	OU	UnTx control	15				
N307	F	WT	OU	UnTx control	15				
N308	F	WT	OU	UnTx control	15				
N300	M	WT	OU	UnTx control	17				
N301	M	WT	OU	UnTx control	17				
N302	F	WT	OU	UnTx control	17				
CCAN	M	WT	OD	UnTx control	37				
CCGS	M	WT	OD	UnTx control	37				
LH14	M	WT	OU	UnTx control	42				
EML31	M	R25*/P463fs	OD	UnTx control	43				
EML27	M	R25*/P463fs	OD	UnTx control	52				
EM346	M	R25*/R25*	OS	UnTx control	89				
N284	F	WT	OS	UnTx control	145				
N269	F	WT	OS	UnTx control	199				

BSS, balanced salt solution; cBEST1, canine transgene; hBEST1, human transgene; Inj., injected; OD, right eye; OS, left eye; OU, bilateral; p.i., postinjection; UnTx, untreated; vg, vector genomes; WT, wild type. cBEST1 mutations: R25*/R25*, p.Arg25Ter-homozygote; P463fs/P463fs, p.Pro463fs-homozygote; R25*/P463fs, p.Arg25Ter/p.Pro463fs-compound heterozygous.

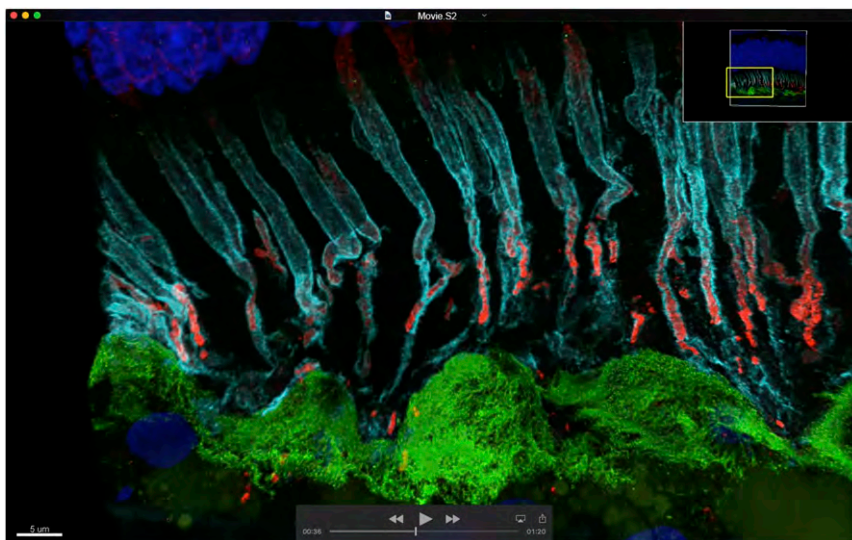
Table S2. List of primary antibodies used for immunohistochemical assessments

Antibody	Dilution	Source
Mouse monoclonal anti-BEST1	1:400	Ab2182; Abcam
Mouse monoclonal anti-EZRIN	1:400	Ab4069; Abcam
Mouse monoclonal anti-RPE65	1:500	NB100-355; Novus Biologicals
Mouse monoclonal anti-RHODOPSIN	1:1,000	MAB5316; Millipore
Rabbit polyclonal anti-hCAR	1:10,000	Courtesy of C. M. Craft, University of Southern California, Los Angeles
Rabbit polyclonal anti-RED/GREEN OPSIN	1:100	AB5405; Millipore
Rabbit polyclonal anti-BLUE OPSIN	1:5,000	AB5407; Millipore
Rabbit polyclonal anti-SLC16A1	1:500	Courtesy of N. J. Philp, Thomas Jefferson University, Philadelphia
Chicken polyclonal anti-CNGB3	1:500	Michigan State University



Movie S1. Three-dimensional rendering of the confocal photomicrograph shown in Fig. 1A. This video demonstrates a 3D reconstruction from a Z-stack image of multicolor immunostaining [hCAR, human cone arrestin (red); EZRIN, RPE apical membrane and microvillar marker (green); PNA lectin selectively binding to the cone-associated insoluble extracellular matrix domains (cyan); DAPI (blue)] capturing the bilayered extracellular compartmentalization of the cone-specific escheatment responsible for normal apposition of RPE-COS in the wild-type canine retina.

[Movie S1](#)



Movie S2. Three-dimensional rendering of the confocal image shown in Fig. 1B, featuring a 3D reconstruction from a Z-stack image of multicolor immunostaining [hCAR (red); EZRIN, RPE apical membrane and microvillar marker (green); PNA lectin selectively binding to the cone-associated insoluble extracellular matrix domains (cyan); DAPI (blue)] assayed in the cBest-mutant (R25*/R25*) retina. Note the multiple abnormalities at the RPE apical surface, particularly the dearth of RPE apical extensions and fragmented cone-IPM, promoting microdetachment in cBest.

[Movie S2](#)